USGS External Research Program Final Report
Award #00-HQ-GR-0060

DEVELOPMENT OF 3D NON-UNIFORM GRID FINITE DIFFERENCE GROUND MOTION SIMULATION METHODOLOGY

Robert W. Graves

URS Corporation
566 El Dorado Street
Pasadena, CA 91101
email: robert_graves@urscorp.com
tel: (626) 449-7650 / fax: (626) 449-3536

March 25, 2002

Development of 3D Non-Uniform Grid Finite Difference Ground Motion Simulation Methodology

Final Report for Award #00-HQ-GR-0060

Robert W. Graves

URS Corporation
566 El Dorado Street
Pasadena, CA 91101
email: robert_graves@urscorp.com
tel: (626) 449-7650 / fax: (626) 449-3536

Abstract

In the first part of this project, I have extended my finite difference simulation code to included the non-uniform grid methodology of Pitarka (1999). The resulting FD algorithm combines the efficiency of the memory optimization procedure (Graves, 1996) with the added benefit of grid size "tuning", which is based on the given velocity model. Changes in grid spacing are restricted to occur uniformly along each of the three coordinate axes. Nonetheless, a significant reduction in memory requirements relative to the fully uniform grid case can be achieved. Likewise, the approach allows for added resolution within the lowest velocity regions of the model. As a demonstration of the algorithm, I have run simulations of the 1992 Landers earthquake using both the uniform and non-uniform methodlogies. With the non-uniform grid approach, the total model size was reduced by almost a factor of two (1.7×10^7 vs. 3.0×10^7 grid points), while at the same time, the smallest grid step was reduced from 0.25 km to 0.15 km within the low velocity basin sediments.

The added efficiency provided by the non-uniform grid methodology allows us to more readily include a robust representation of anelastic attenuation in the time-stepping algorithm. With this goal, in mind in the second part of this project, we have analyzed the stability and accuracy of the coarse-grain memory variable technique used for viscoelastic wave field simulations. Here, it is shown that the general behavior of the coarse-grain system is well described by effective parameters (M_E and Q_E) that are derived from the harmonic average of the moduli over the volume of the coarse-grain cell. In addition, the

use of these effective parameters proves essential for analyzing the performance and accuracy of the coarse-grain system for low values (less than about 20) of Q. By analyzing the functional form of the viscoelastic modulus, we derive a necessary stability condition for the coarse-grain system, which requires that the weighting coefficients be bounded between zero and one. Specifying the weights using the approach of Day and Bradley (2001) satisfies this condition for Q values of about 3 and larger; however, using unconstrained optimization techniques will often produce weights that violate this condition at much higher Q values. We also derive an improved formulation of the original coarse-grain methodology called the element specific modulus (ESM) formulation. In the ESM formulation, each element of the coarse-grain cell uses a different unrelaxed modulus and we provide theoretical expressions for these unrelaxed moduli. We demonstrate that the accuracy of the coarse-grain system for Q values lower than about 20 is significantly increased by using the ESM formulation. Furthermore, the cost of implementing the ESM formulation is virtually identical to that of the original formulation. Finally, we present a technique for optimizing the accuracy of the coarse-grain system for very low Q values. The optimization of the coarse-grain system requires the use of the effective quality factor (Q_E), and we demonstrate that using conventional optimization techniques that do not employ the effective parameter Q_E will actually degrade the accuracy of the resulting coarse-grain system.

Publications and Presentations

Graves, R. W. and S. M. Day (2002). Stability and accuracy analysis of coarse-grain viscoelastic simulations, *submitted to Bull. Seism. Soc. Am.*

Graves, R. W. (2001). Long period ground motions in the San Bernardino region for hypothetical San Andreas and San Jacinto earthquakes, *Eos. Trans. AGU*, **82**(47), Fall Meet. Suppl., Abstract S32D-09.

Graves, R. W. and D. J. Wald (2001). Observed and simulated strong ground motions in the San Bernardino basin region, *Seism.. Res. Lett.*, **72**(2), p. 284.

Graves, R. W. and D. J. Wald (2000). Observed basin response and 3D ground motion simulations for the 1999 Hector Mine earthquake, *Eos. Trans. AGU*, **81**(48), Fall Meet. Suppl., Abstract S52A-15.

Ground Motion Simulations of the 1992 Landers Earthquake Using Non-Uniform Grid Finite Differences

Robert W. Graves

URS Corporation
566 El Dorado Street
Pasadena, CA 91101
robert_graves@urscorp.com

Introduction

In this project, I have extended my finite difference simulation code to included the non-uniform grid methodology of Pitarka (1999). The resulting FD algorithm combines the efficiency of the memory optimization procedure (Graves, 1996) with the added benefit of grid size "tuning", which is based on the given velocity model. Changes in grid spacing are restricted to occur uniformly along each of the three coordinate axes. Nonetheless, a significant reduction in memory requirements relative to the fully uniform grid case can be achieved. Likewise, the approach allows for added resolution within the lowest velocity regions of the model. As a demonstration of the algorithm, I have run simulations of the 1992 Landers earthquake using both the uniform and non-uniform methodlogies. With the non-uniform grid approach, the total model size was reduced by almost a factor of two (1.7×10^7 vs. 3.0×10^7 grid points), while at the same time, the smallest grid step was reduced from 0.25 km to 0.15 km within the low velocity basin sediments.

Simulations Results

Figure 1 shows the model region used for the simulations. The Landers source is represented as a three segment fault model. The rupture model used in the simulations is from Wald and Heaton (1994), and includes a detailed description of the temporal and spatial heterogeneity of the rupture process. The velocity model is from the SCEC V1 3D velocity structure. Most of the model is represented as a 1D velocity structure, which is given by Hadley and Kanamori (1977). The westernmost portion of the model covers the San Bernardino basin region. The San Bernardino basin is a wedge-shaped structure which

lies between the San Andreas fault on the north and the San Jacinto fault to the south. Maximum thickness of sediments within the basin are greater than 1 km.

Ground motions recorded in the San Bernardino area for the Landers and Big Bear earthquake sequences show significant basin response effects. These effects include elevated amplitudes and extended durations of shaking relative to sites just outside of the basin (e.g., Frankel, 1994).

For the uniform grid simulations, I used a grid step of 0.25 km and a minumum shear wave velocity of 600 m/s. This gives a maximum frequency resolution of about 0.5 Hz. For the non-uniform grid calculations, the minimum shear velocity remains at 600 m/s; however, the grid spacing in the lowest velocity regions is reduced to 0.15 km. Not only does this raise the maximum frequency resolution to about 0.8 Hz, it also allows for a more detailed representation of the shallow velocity structure within the basin.

Figures 2a - 2u compare three component simulated time histories at a number of stations for the two simulations methodologies. The times histories are ground velocity (cm/s), and they have all been low-pass filtered at 0.5 Hz. For sites located outside of the basin, the two methodologies produce very similar waveforms. This suggests that the source and 1D velocity structure are accurately represented by the non-uniform grid methodology. For sites within the basin, the two methodologies produce somewhat different results. These differences can be attributed to the differences in the resulting 3D velocity structures that are used by the two methods. That is, even though the original velocity model is the same, the sampling of the model with different grid sizes actually results in two different computational models. In effect, this can be thought of as spatially aliasing the original velocity structure. I confirmed that the non-uniform grid code does reproduce exactly the same results as the uniform grid code by running a test model in which both methods used identical 3D velocity structures (albeit with differing grid steps).

Conclusions

I have successfully implemented the non-uniform grid metholodology of Pitarka (1999) in my FD simulation software. Performance tests indicate a substantial increase in efficiency is realized using the new methodology. A comparison of simulations results for the 1992

Landers earthquake shows that in addition to the increased efficiency of the non-uniform grid technique, spatial aliasing of the input velocity structure can be reduced as well. The non-uniform methodology has also been applied to the modeling of the 1999 Hector Mine earthquake (Graves and Wald, 2000), and to the modeling of ground motions for scenario earthquakes (Graves, 2001).

References

Frankel, A. (1994). Dense array recordings in the San Bernardino Valley of Landers-Big Bera aftershocks: basin surface waves, Moho reflections, and three dimensional simulations, *Bull. Seism. Soc. Am.*, **84**, 613-624.

Graves, R. W. (1996). Simulating seismic wave propagation in 3D elastic media using staggered-grid finite-differences, *Bull. Seism. Soc. Am.*, **86**, 1091-1106.

Graves, R. W. (2001). Long period ground motions in the San Bernardino regions for hypothetical San Andreas and San Jacinto earthquakes, *Eos. Trans. AGU*, **82**(47), Fall Meet. Suppl., Abstract S32D-09.

Graves, R. W. and D. J. Wald (2000). Observed basin response and 3D ground motion simulations for the 1999 Hector Mine earthquake, *Eos. Trans. AGU*, **81**(48), Fall Meet. Suppl., Abstract S52A-15.

Hadley, D. M. and H. Kanamori (1977). Seismic structure of the Transverse Ranges, California, *Geol. Soc. Am. Bull.*, **88**, 1469-1478.

Pitarka, A. (1999). 3D elastic finite-difference modeling of seismic motion using staggered grids with nonuniform spacing, *Bull. Seism. Soc. Am.*, **89**, 54-68.

Wald, D. J. and T. H. Heaton (1994). Spatial and temporal distribution of slip for the 1992 Landers, California, earthquake, *Bull. Seism. Soc. Am.*, **84**, 668-691.

San Bernardino Basin Model

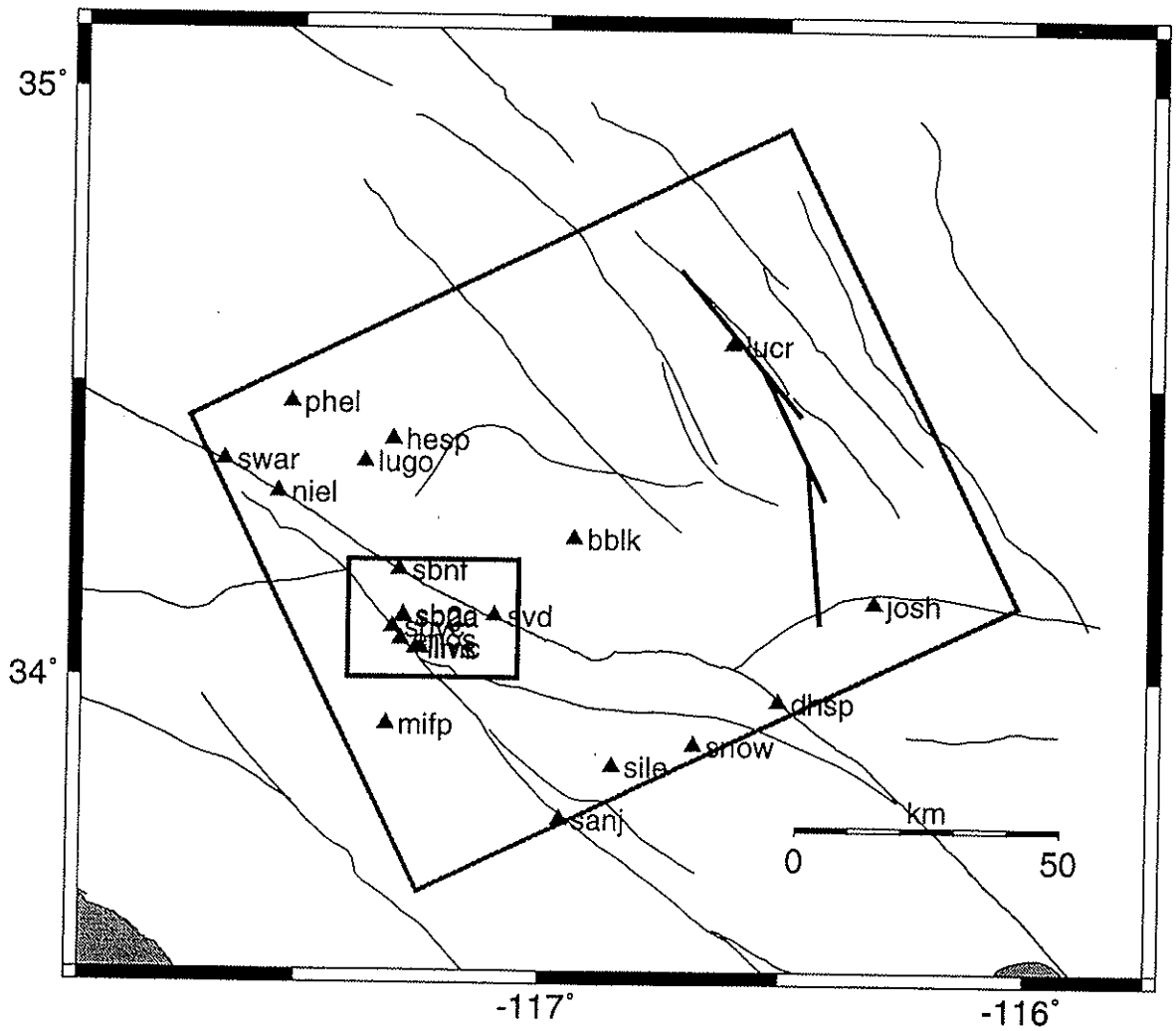

Figure 1: FD model region used in the simulation of the 1992 Landers earthquake. The black rectangle at the left of the model is the San Bernardino basin region.

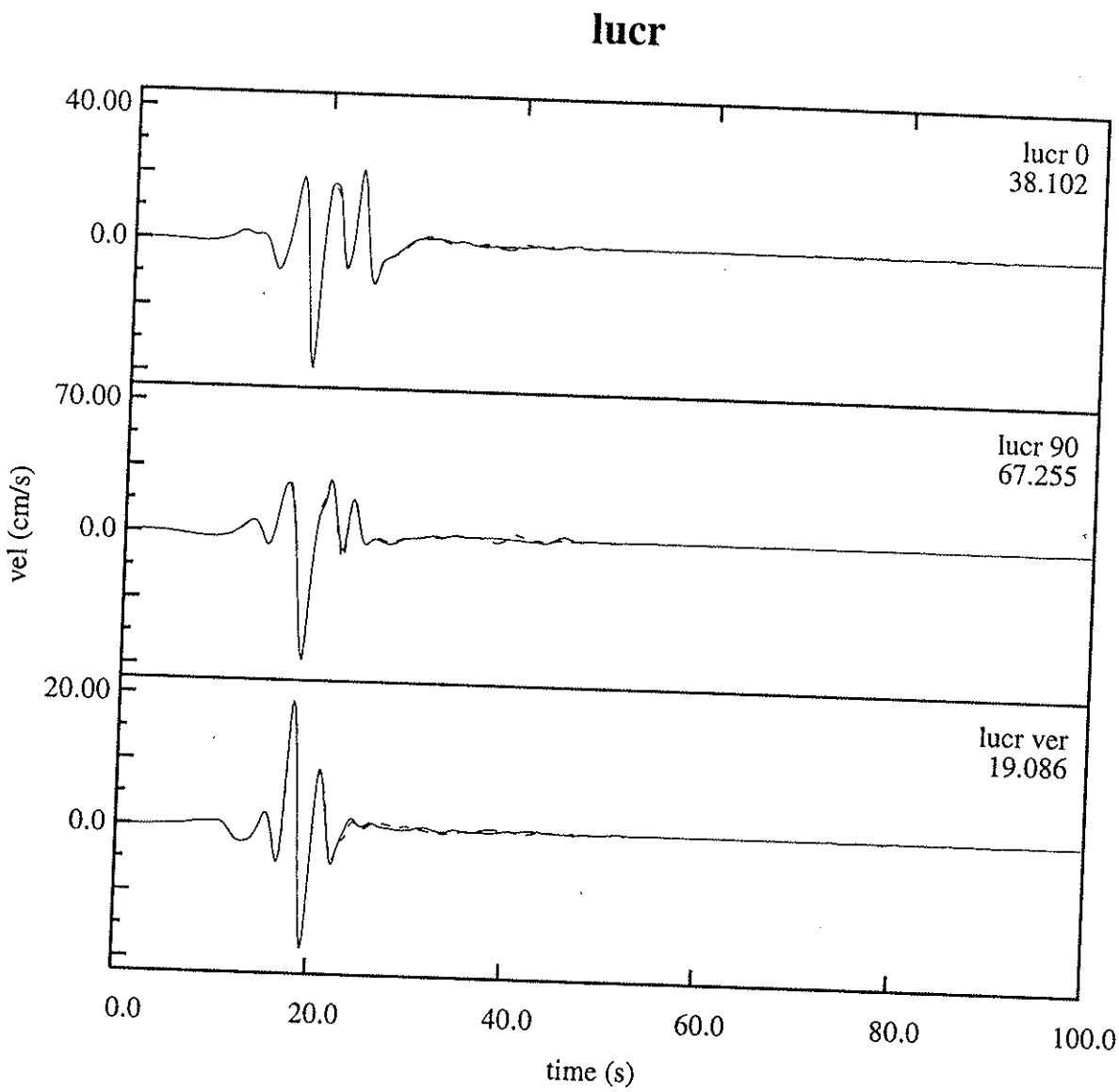

Figure 2a: Comparison of simulation results at stations lucr for uniform (dashed line) and non-uniform (solid line) grid FD calculations of the Landers EQ.

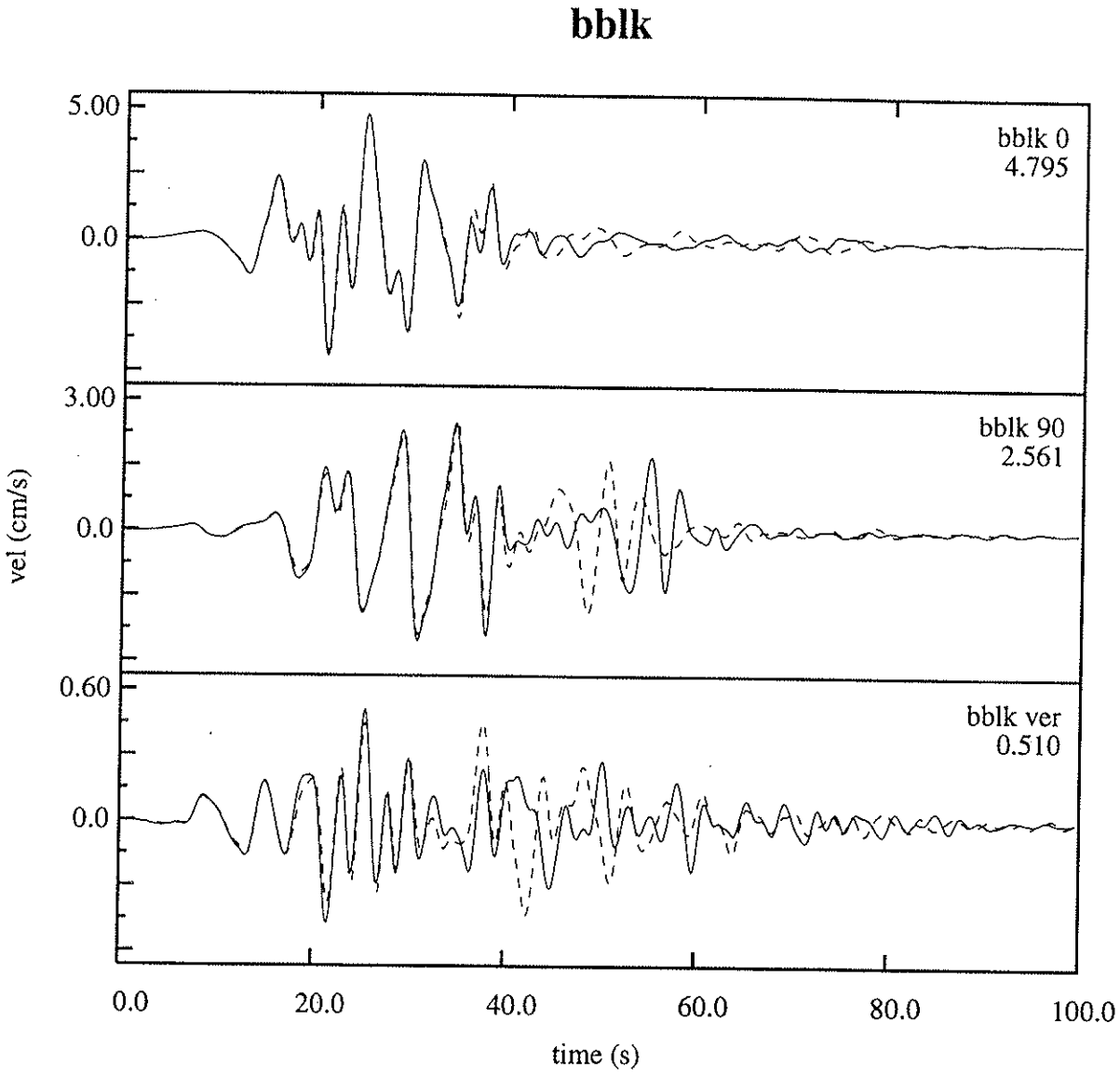

Figure 2b: Same as Figure 2a, except for station bblk.

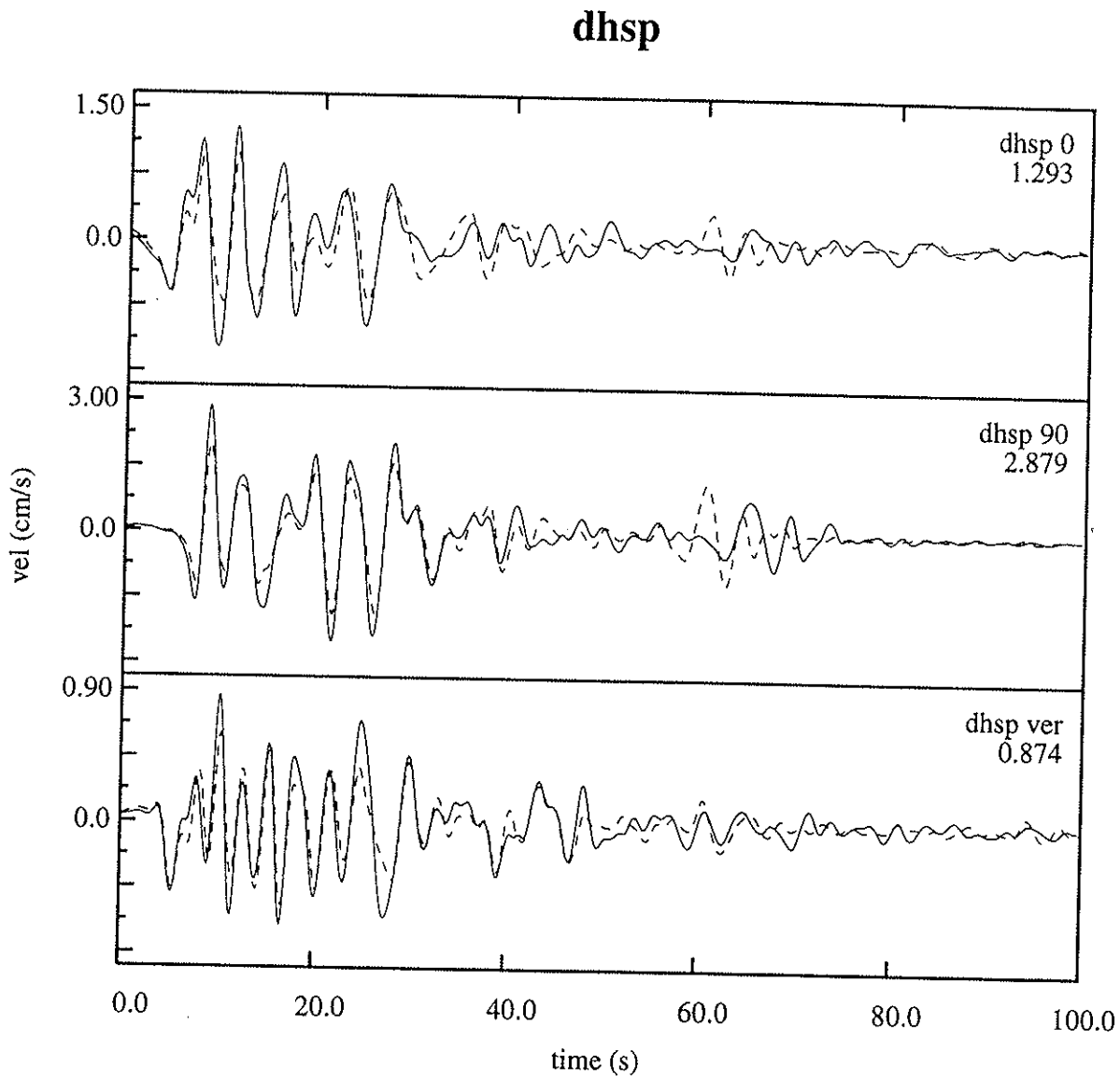

Figure 2c: Same as Figure 2a, except for station dhsp.

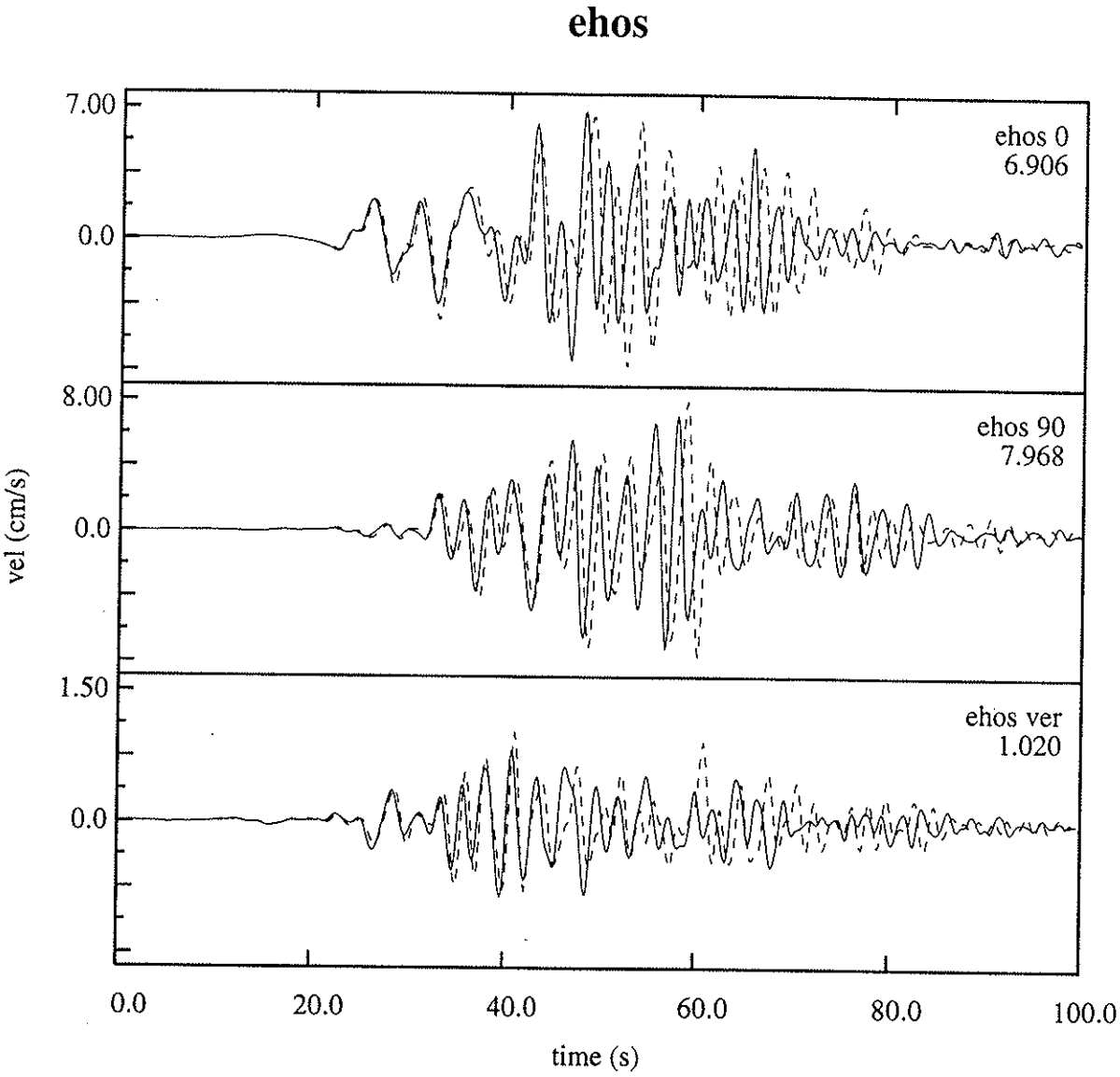

Figure 2d: Same as Figure 2a, except for station ehos.

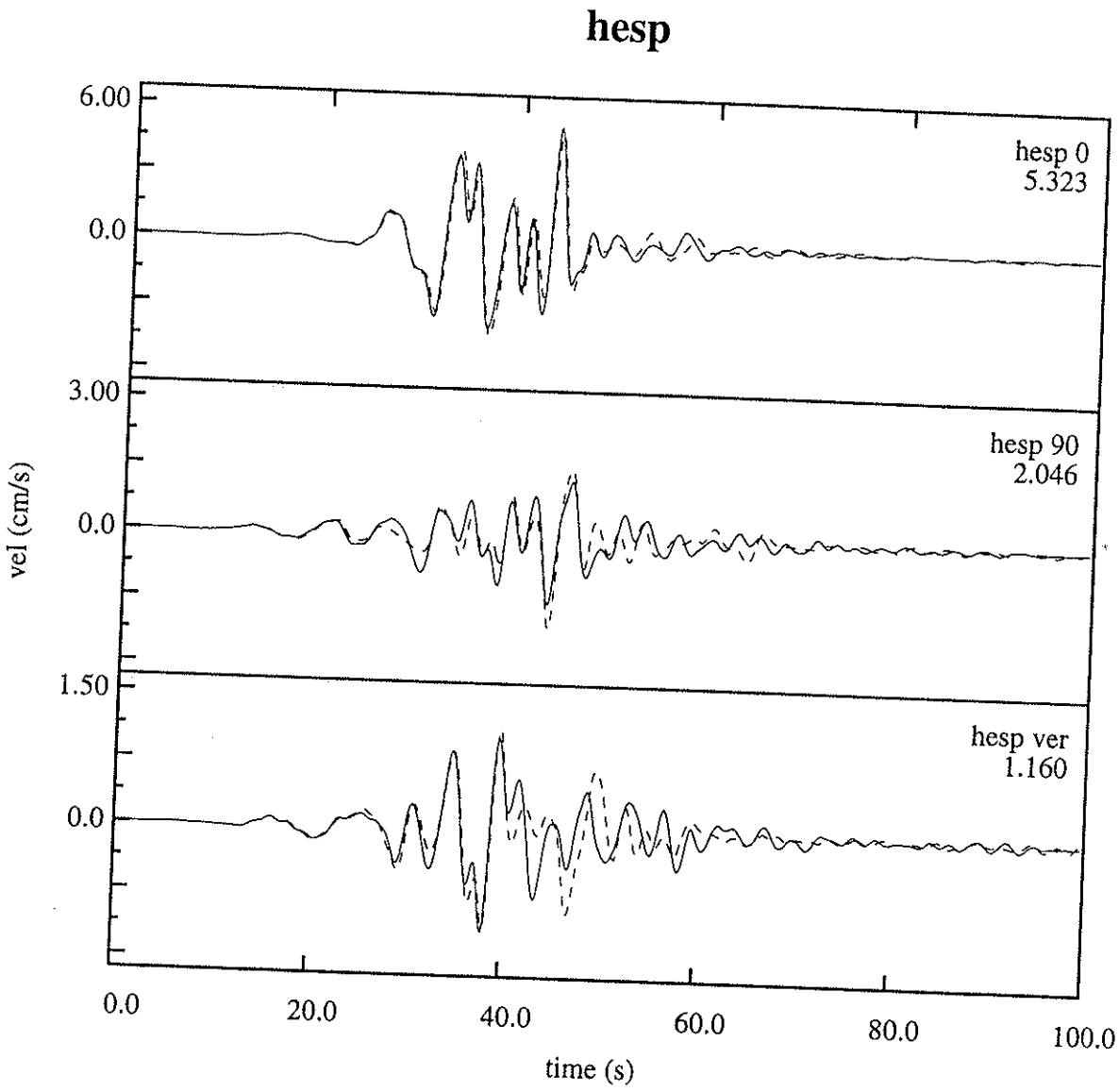

Figure 2e: Same as Figure 2a, except for station hesp.

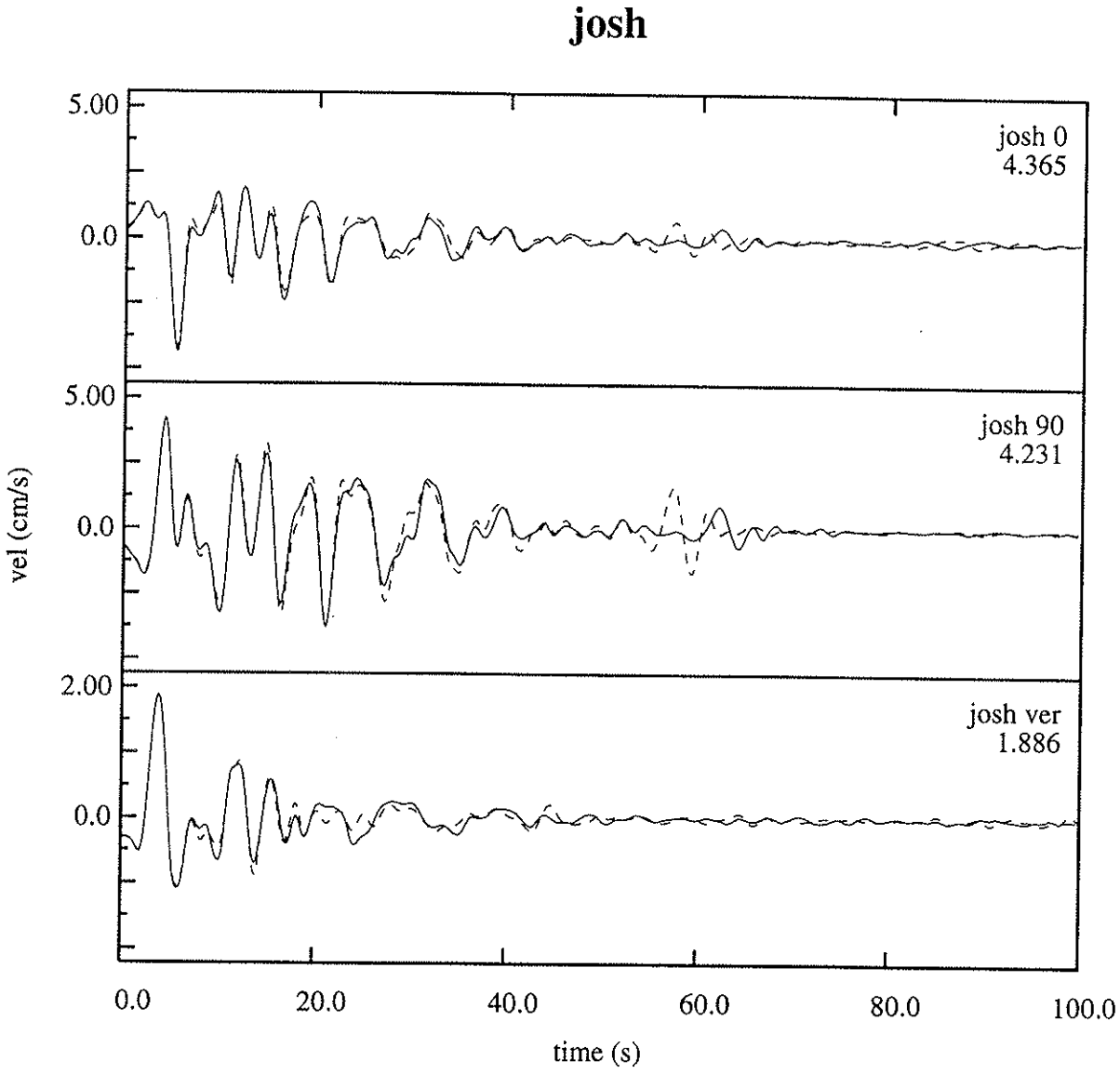

Figure 2f: Same as Figure 2a, except for station josh.

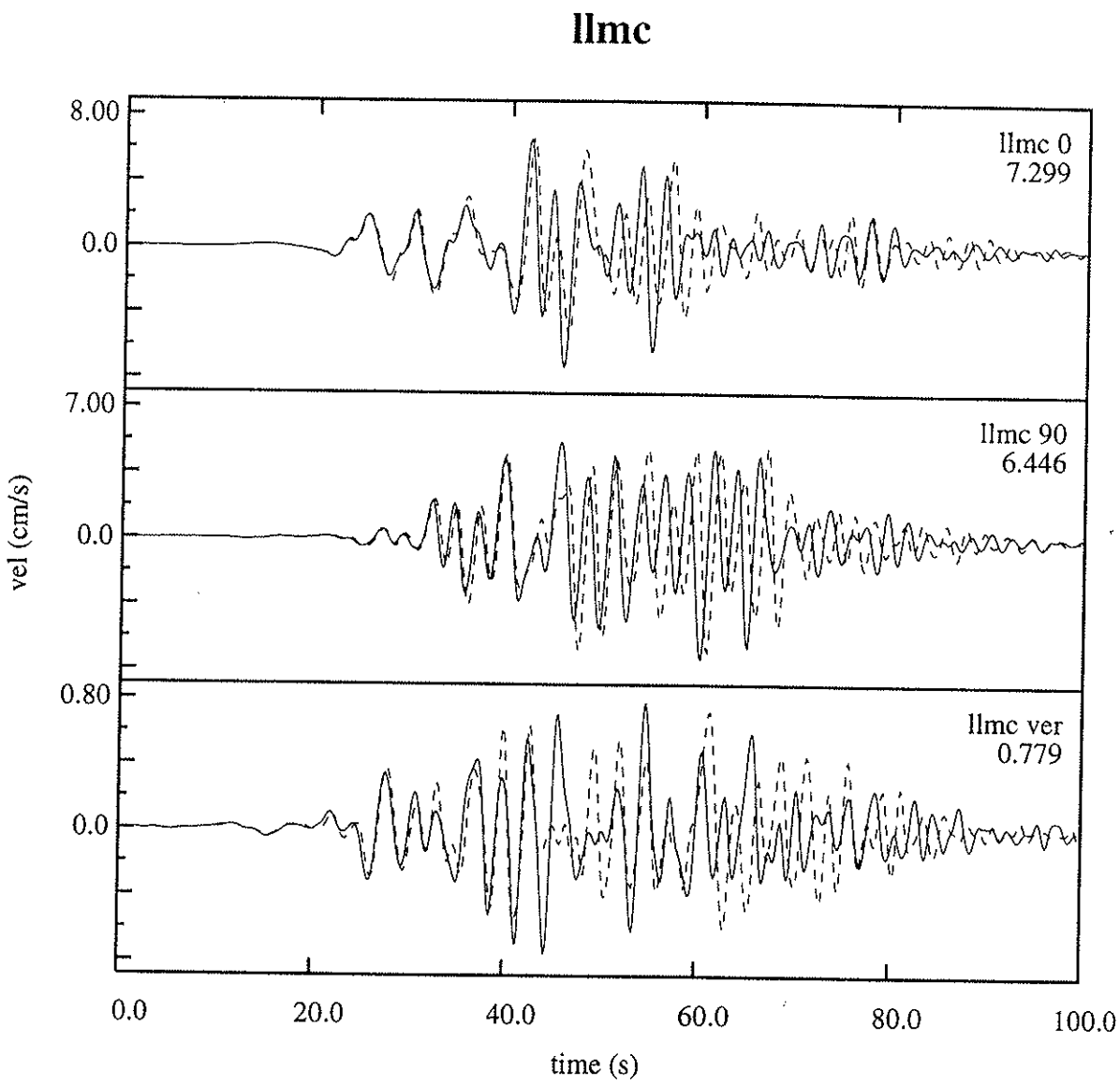

Figure 2g: Same as Figure 2a, except for station llmc.

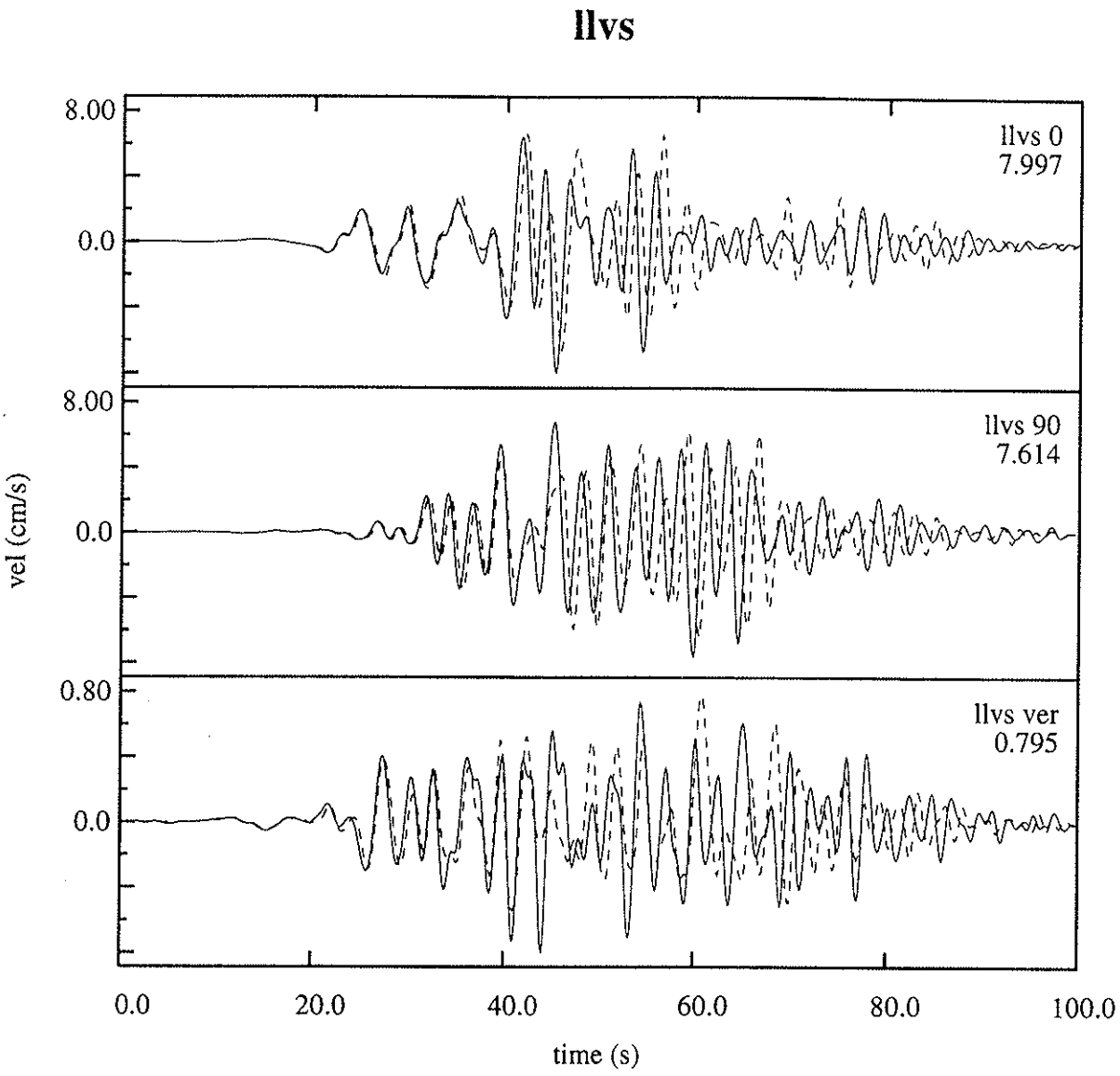

Figure 2h: Same as Figure 2a, except for station llvs.

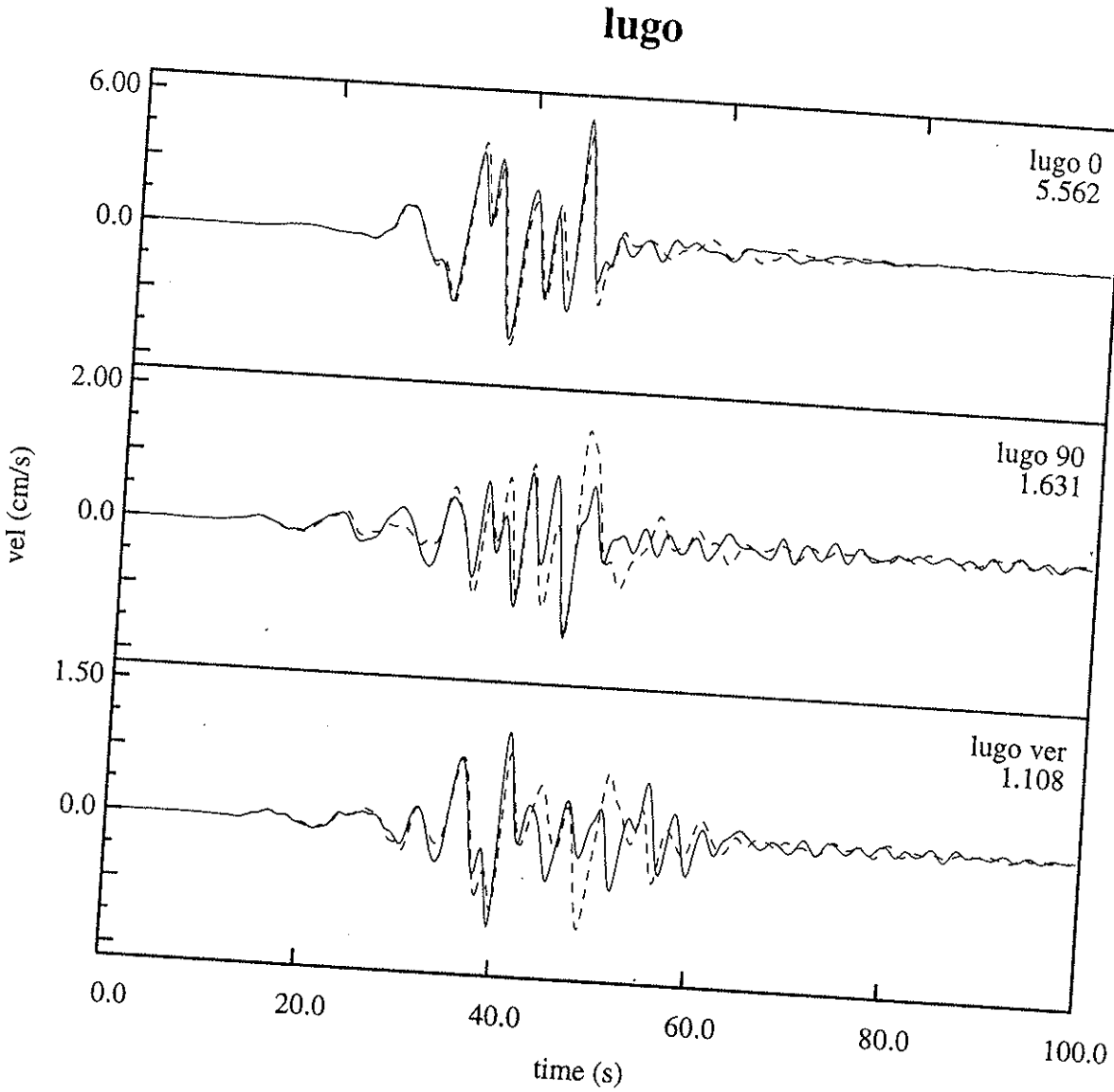

Figure 2i: Same as Figure 2a, except for station lugo.

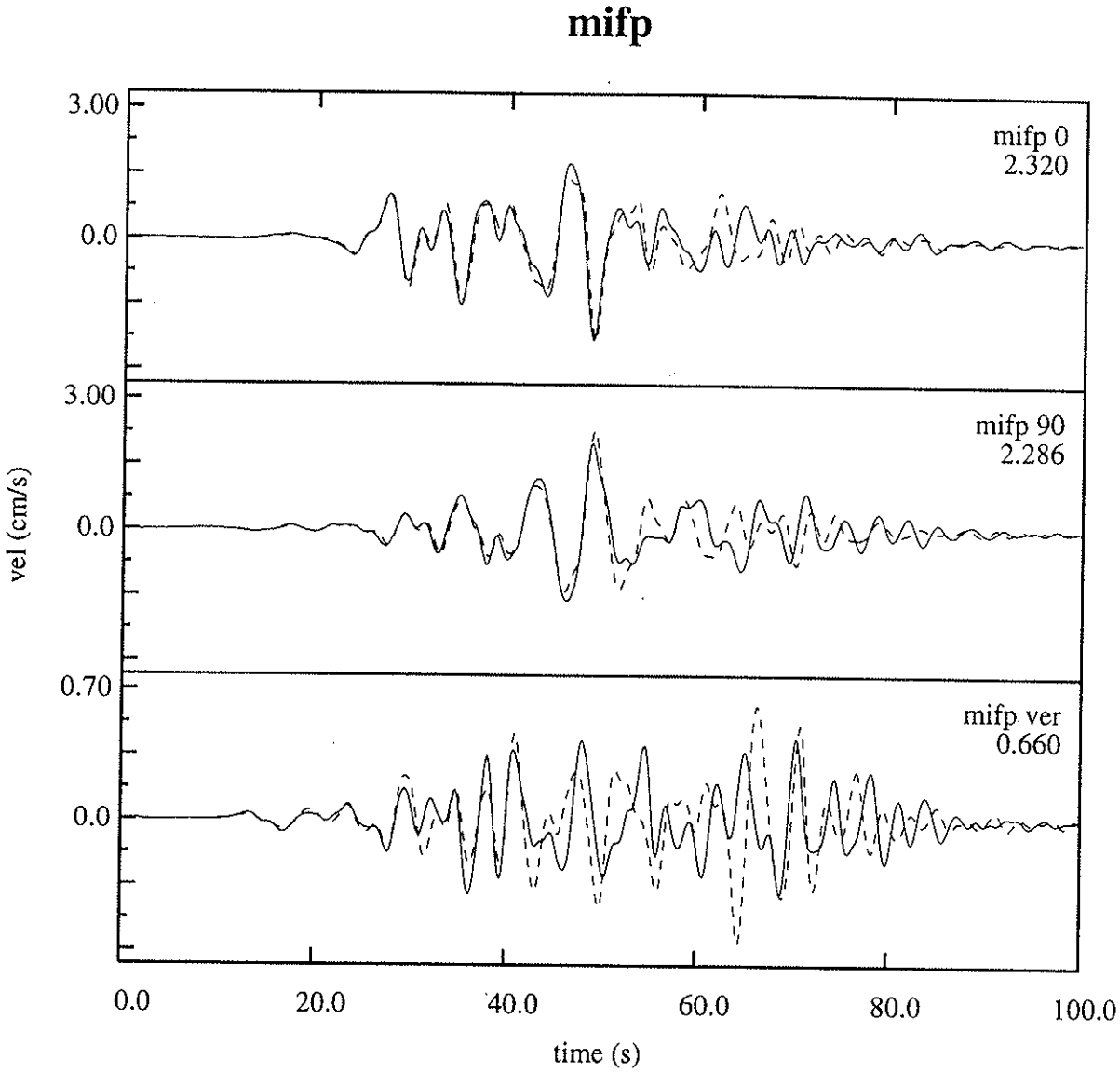

Figure 2j: Same as Figure 2a, except for station mifp.

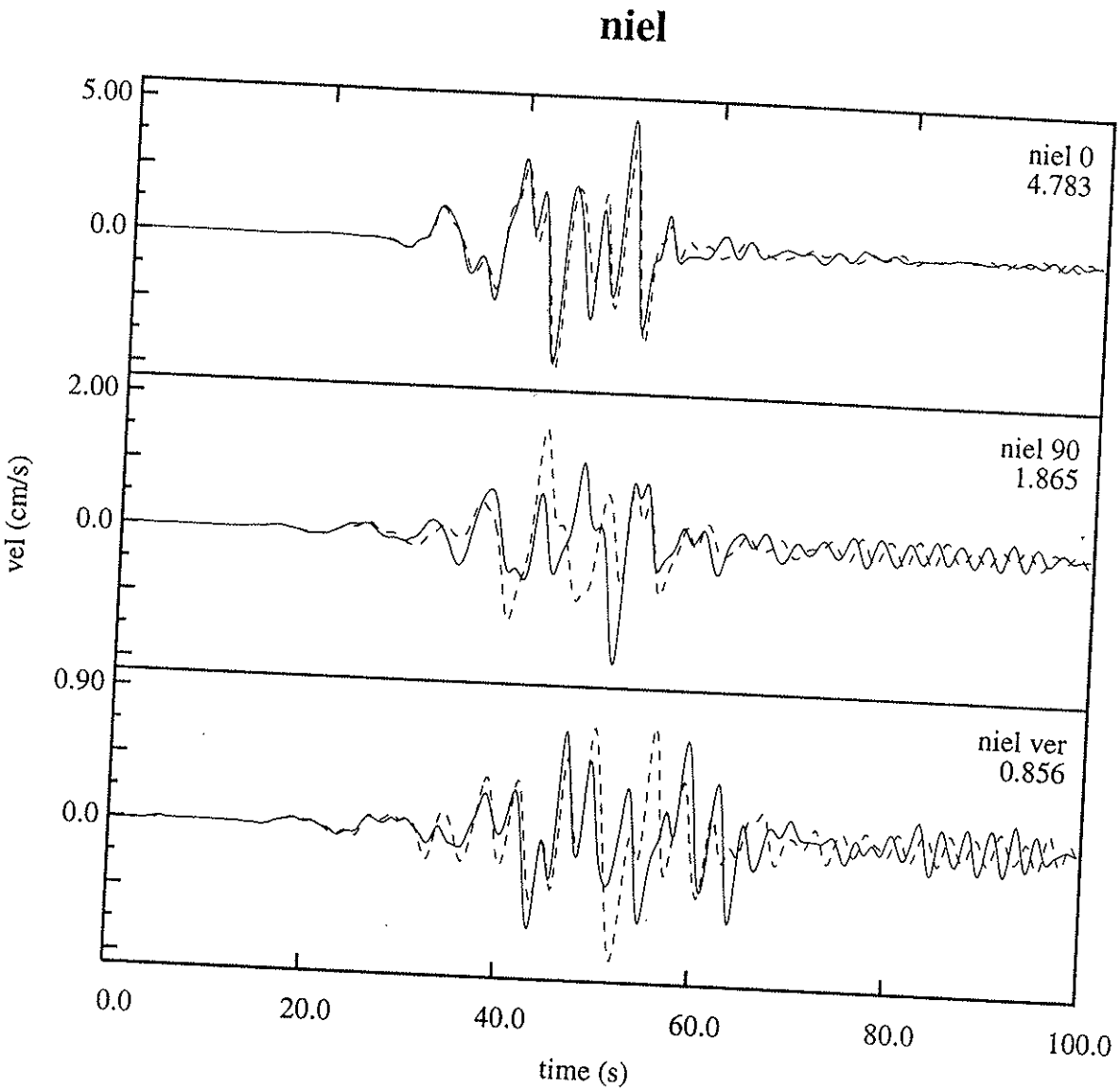

Figure 2k: Same as Figure 2a, except for station niel.

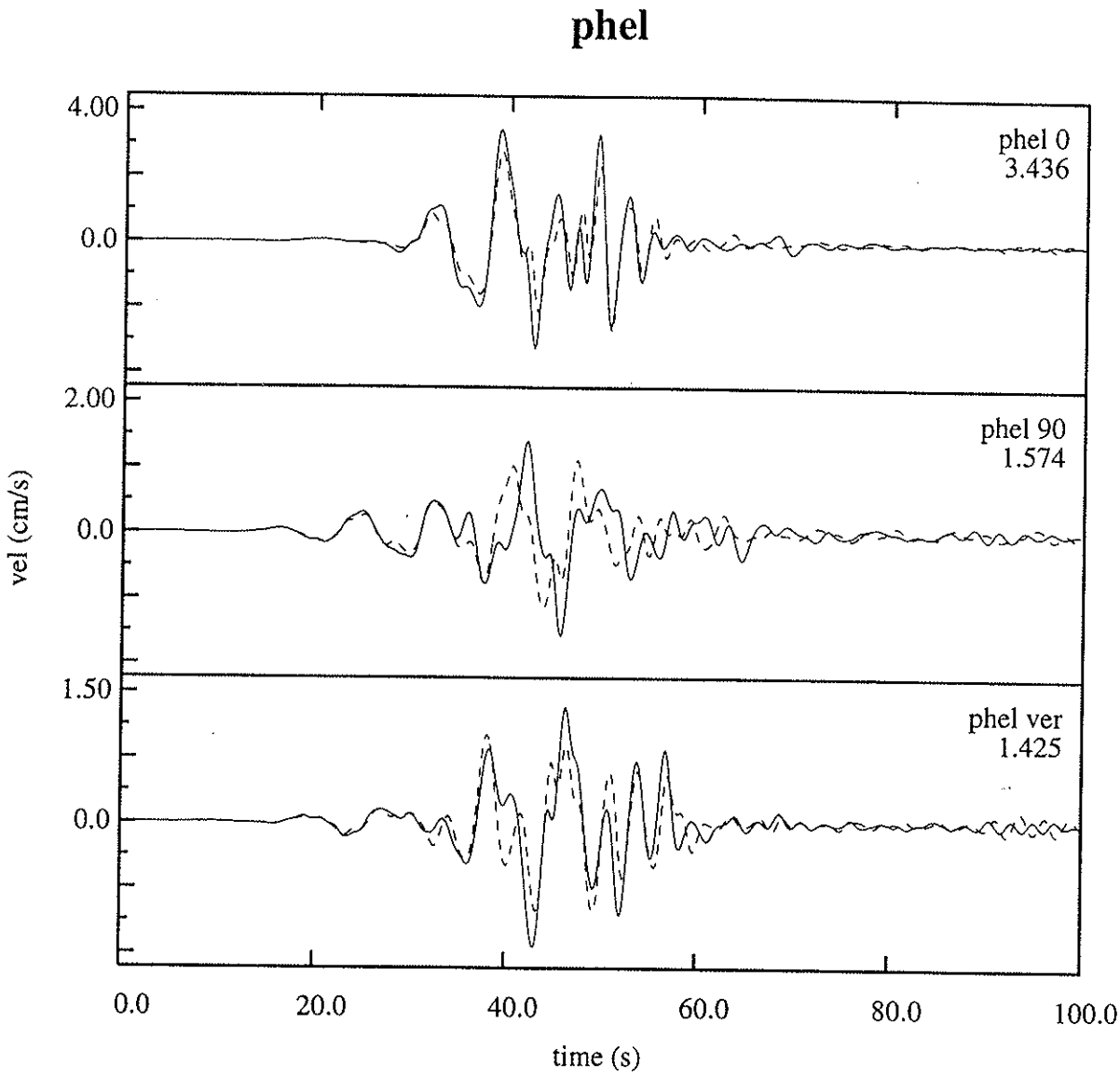

Figure 2l: Same as Figure 2a, except for station phel.

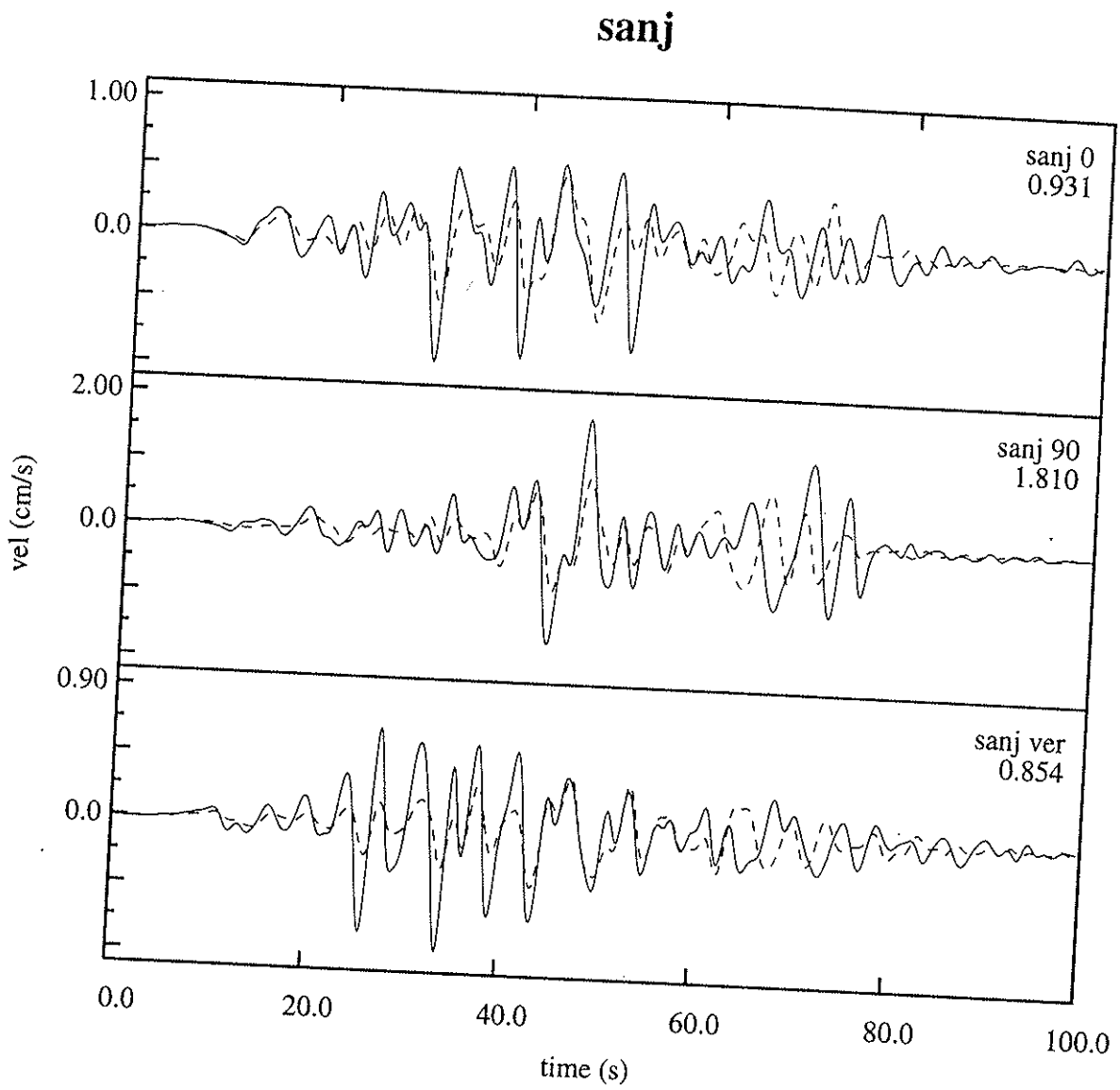

Figure 2m: Same as Figure 2a, except for station sanj.

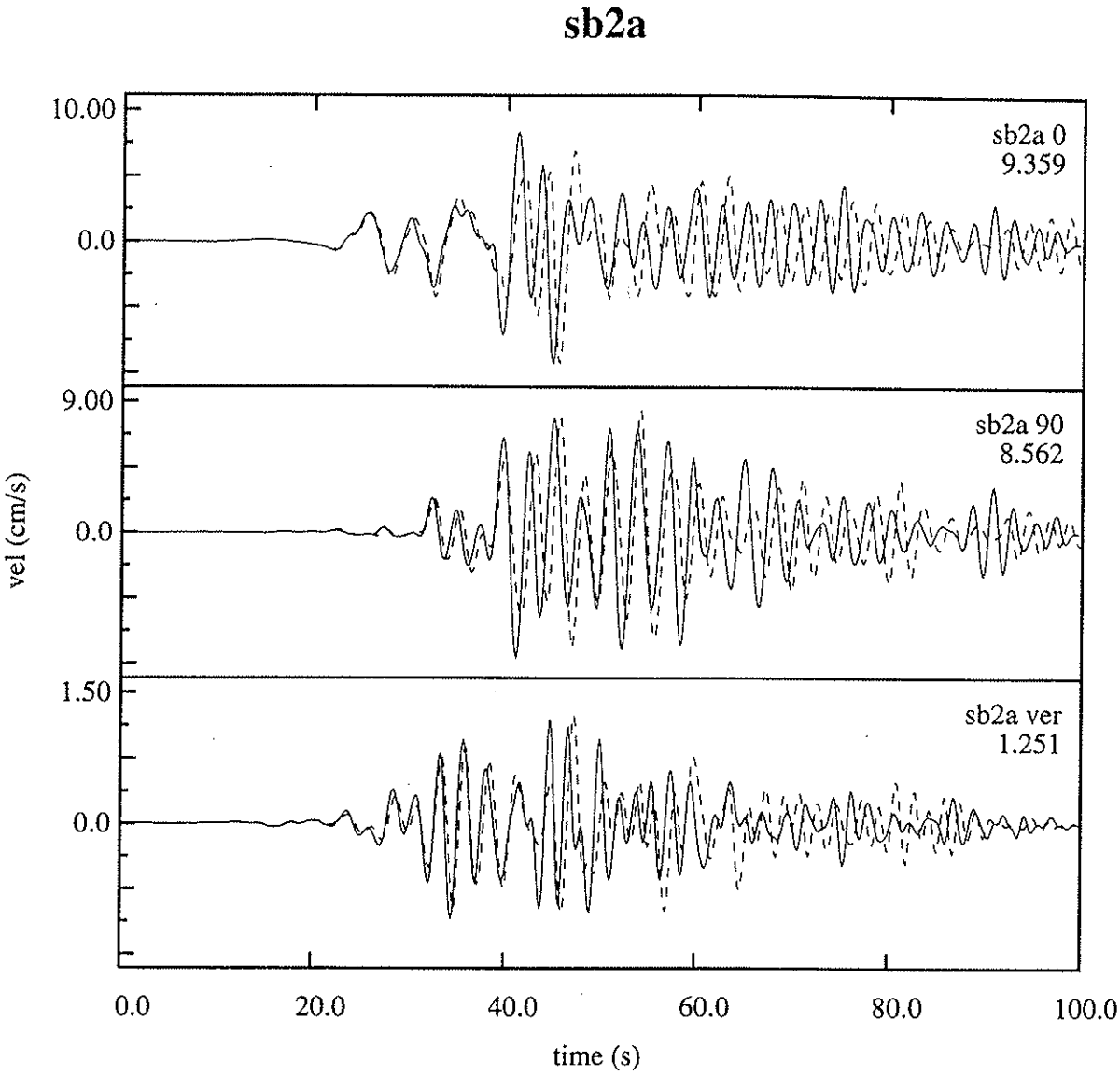

Figure 2n: Same as Figure 2a, except for station sb2a.

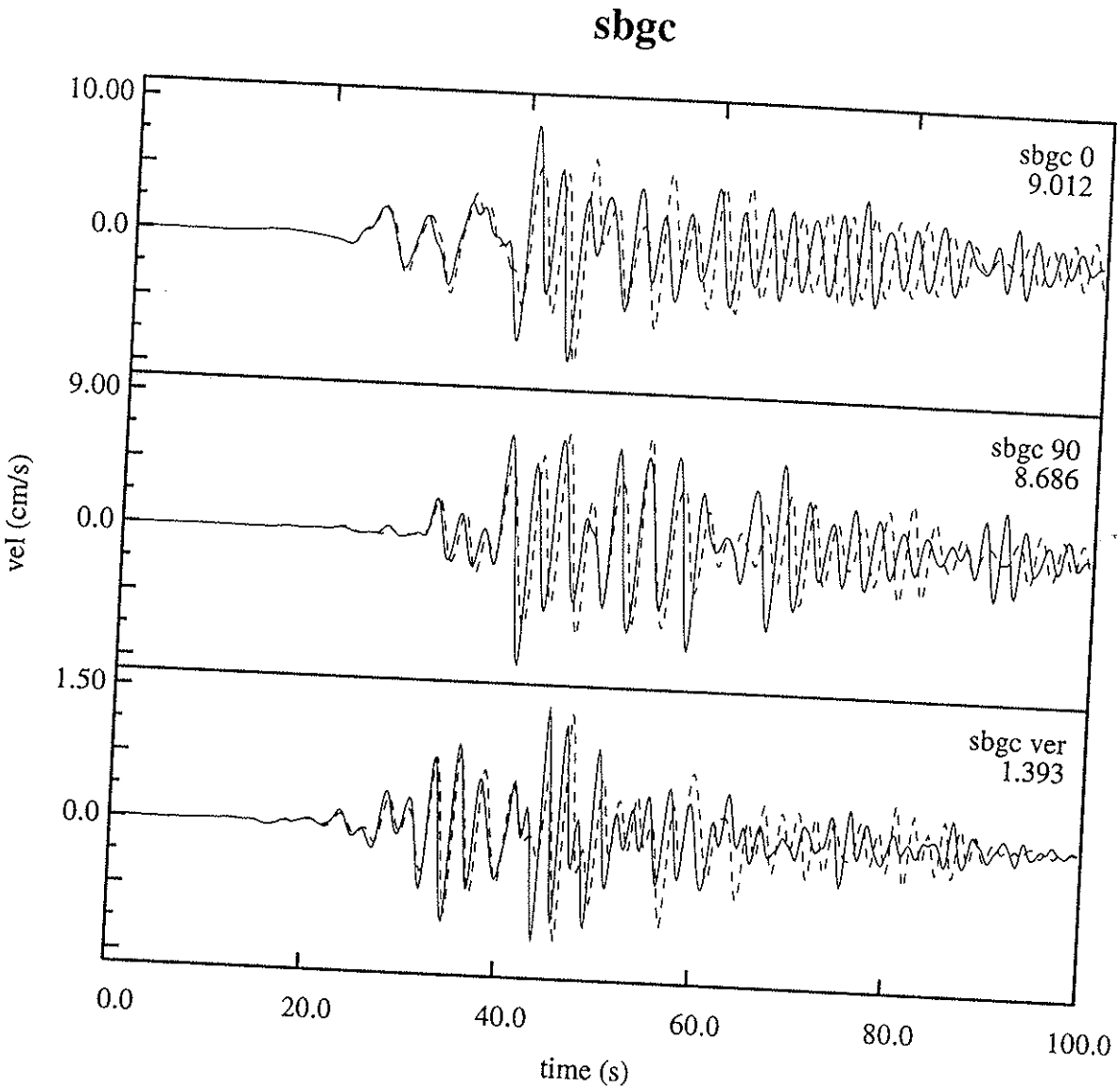

Figure 2o: Same as Figure 2a, except for station sbgc.

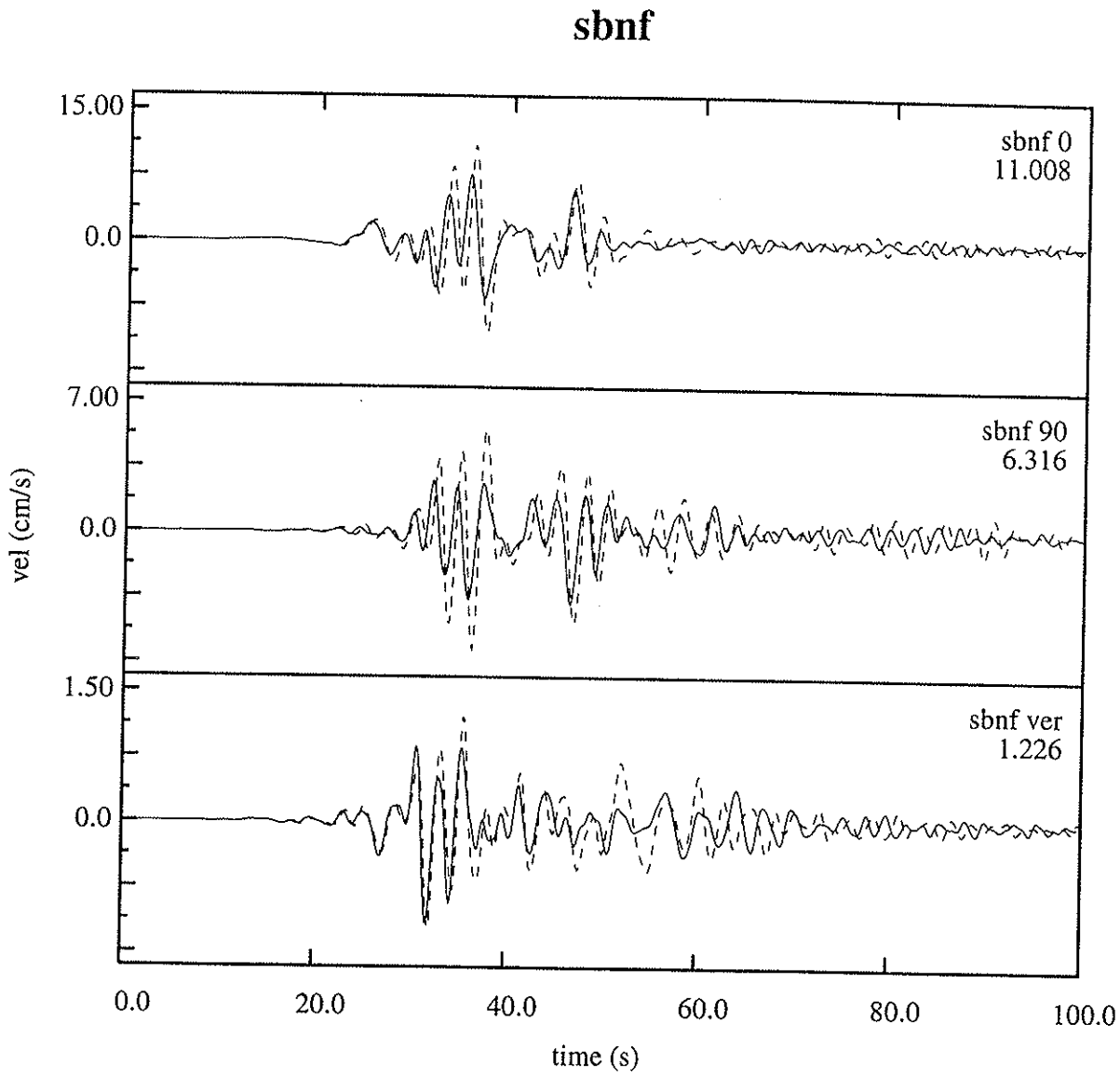

Figure 2p: Same as Figure 2a, except for station sbnf.

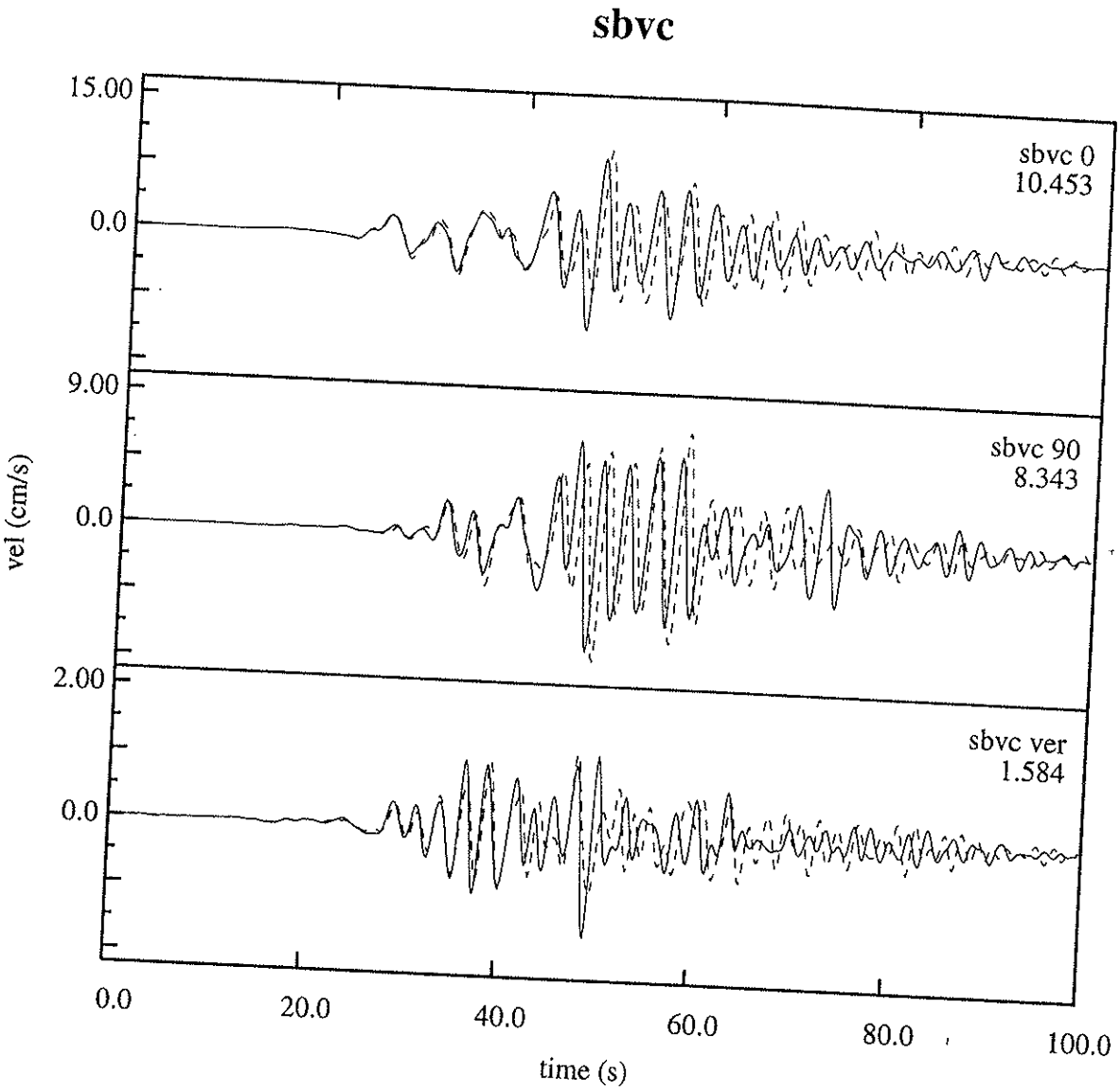

Figure 2q: Same as Figure 2a, except for station sbvc.

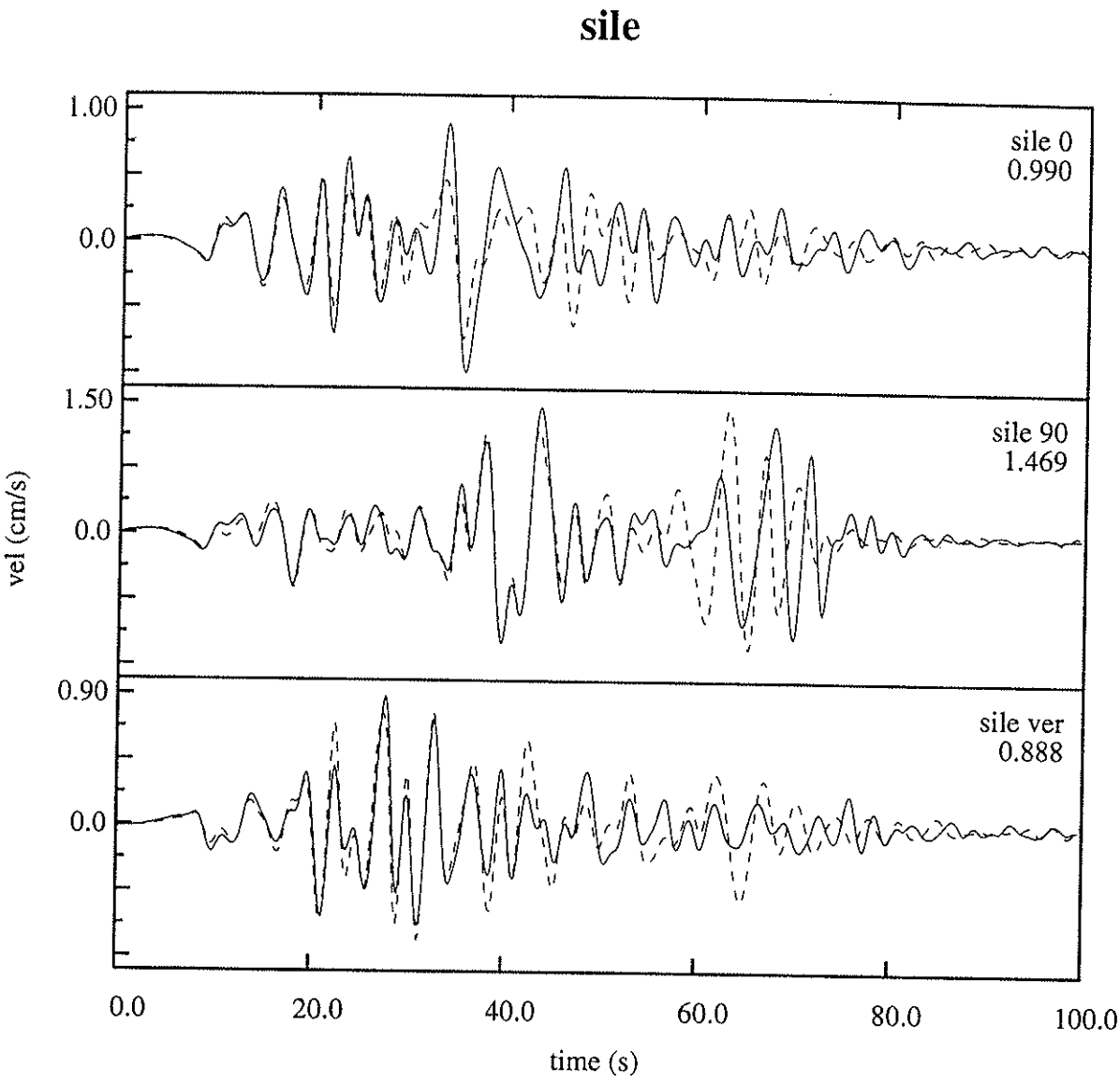

Figure 2r: Same as Figure 2a, except for station sile.

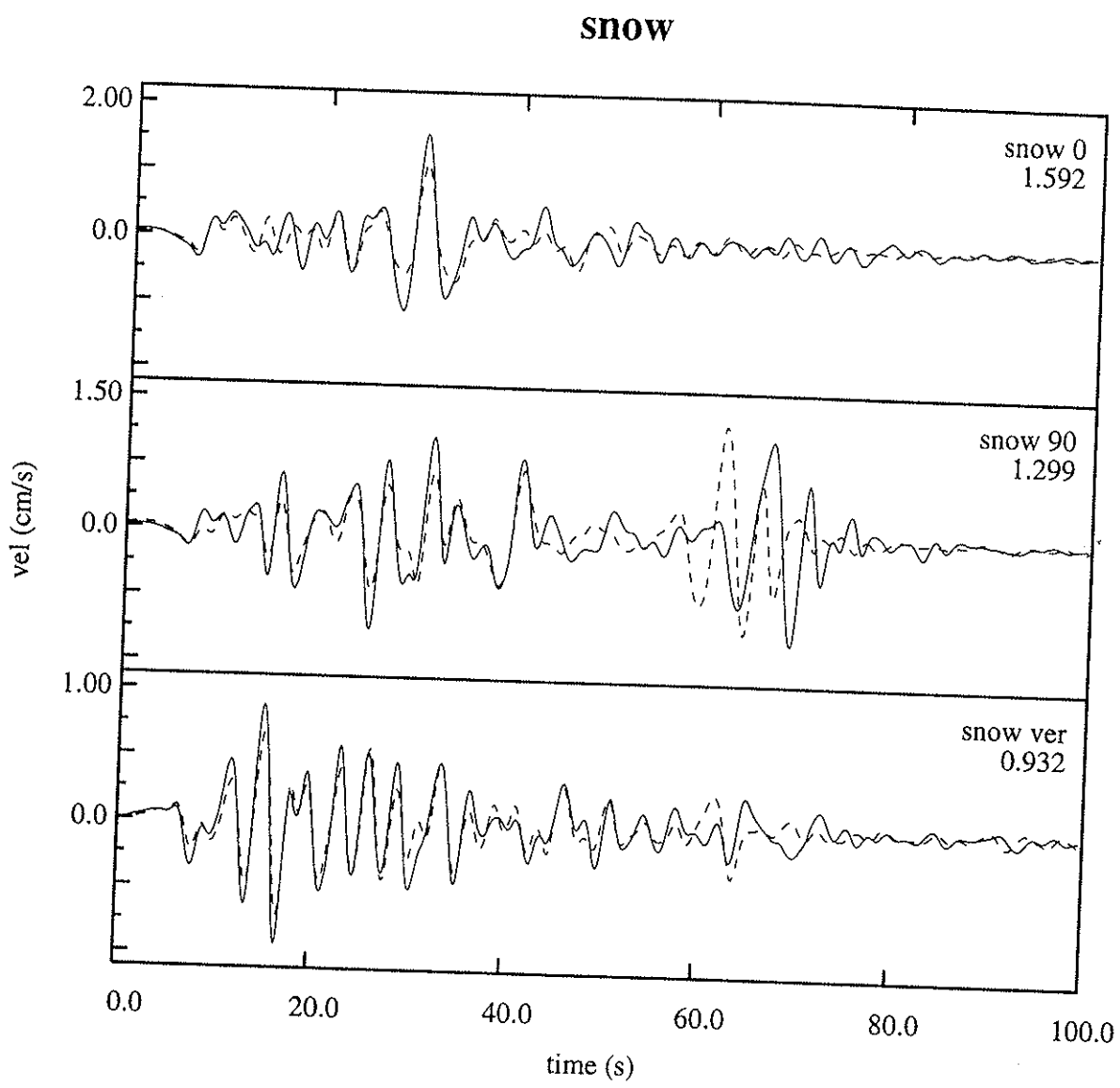

Figure 2s: Same as Figure 2a, except for station snow.

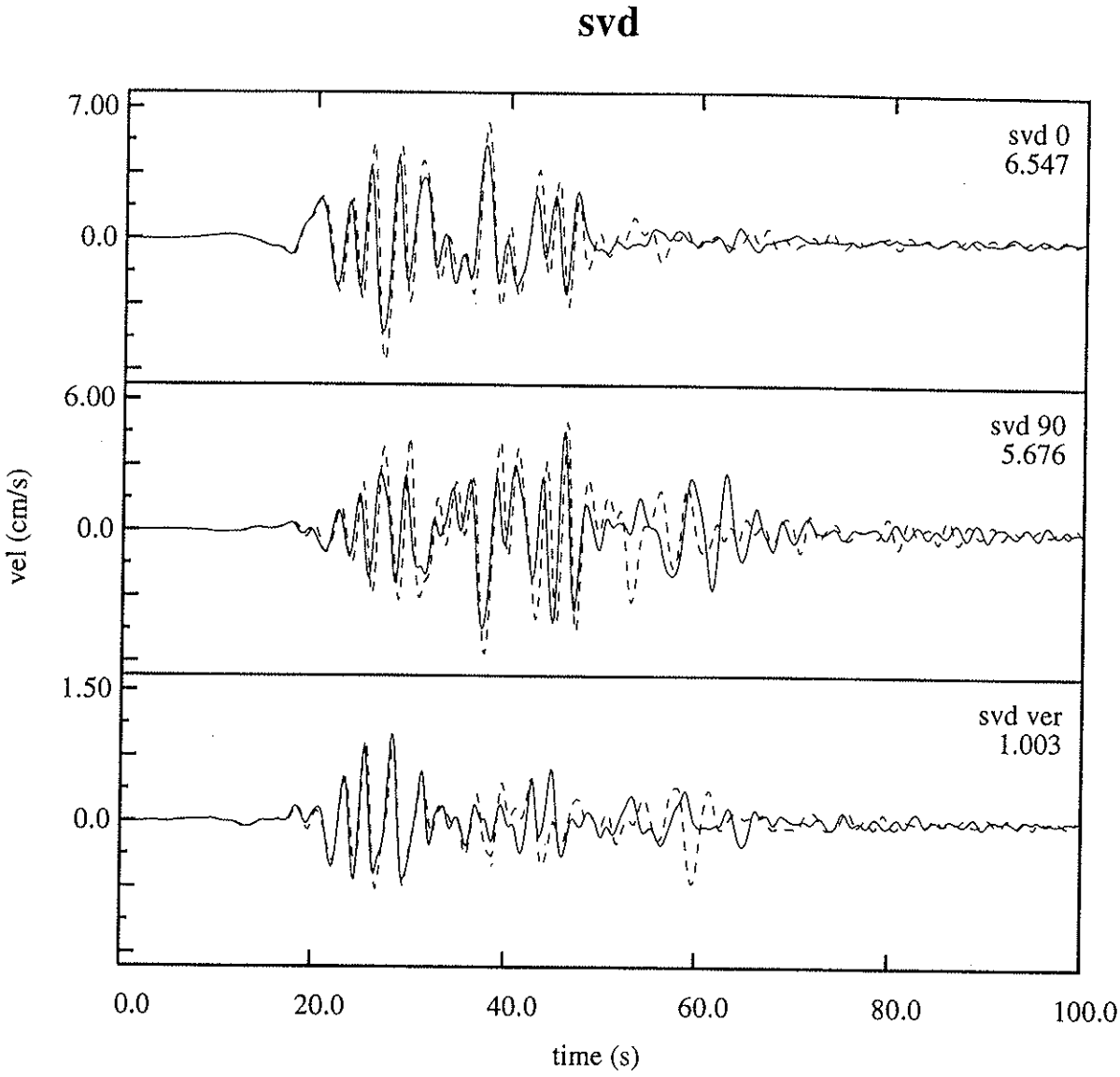

Figure 2t: Same as Figure 2a, except for station svd.

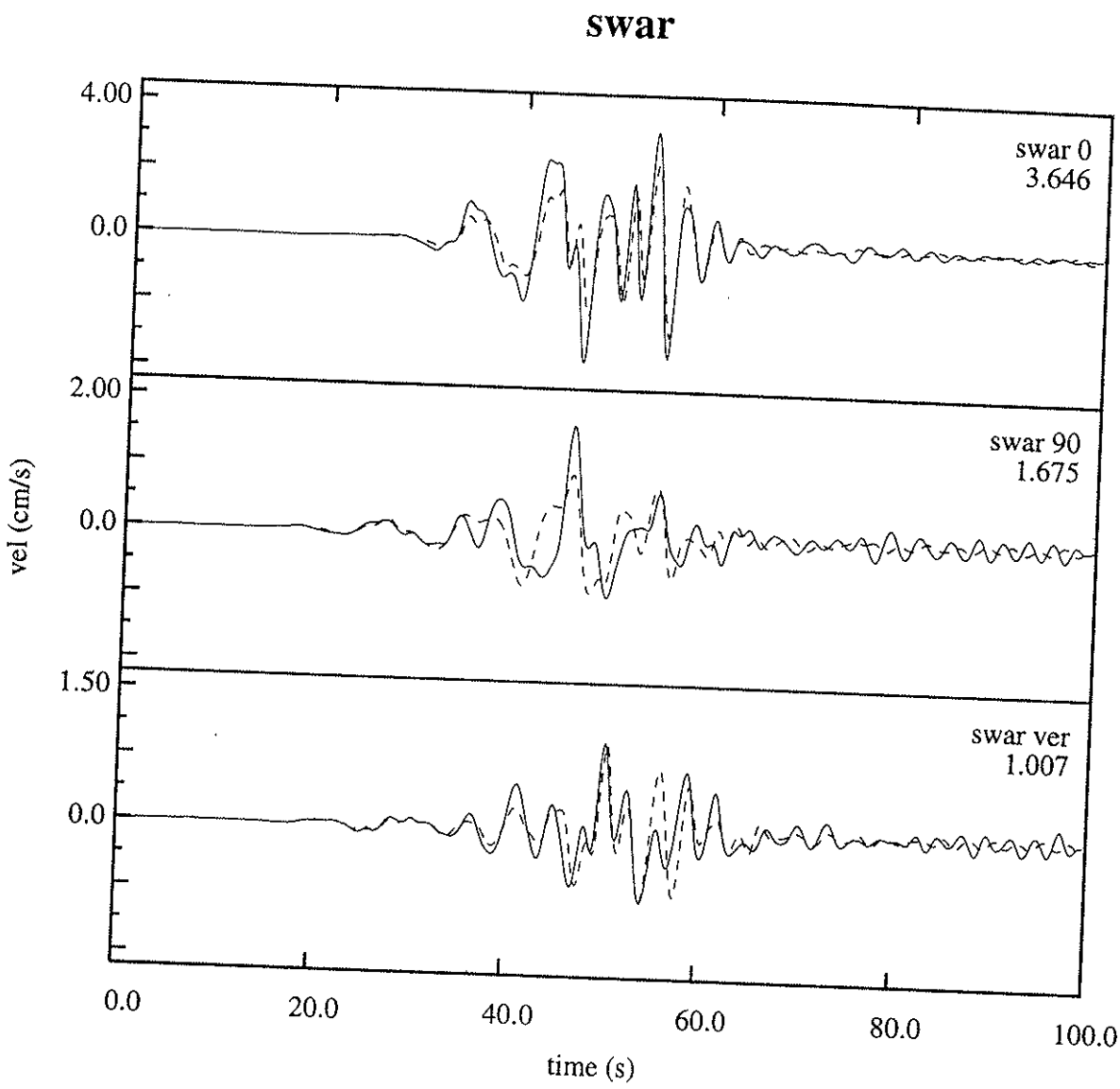

Figure 2u: Same as Figure 2a, except for station swar.

Stability and Accuracy Analysis of Coarse-Grain Viscoelastic Simulations

Robert W. Graves[1] and Steven M. Day[2]

[1]URS Corporation
566 El Dorado Street
Pasadena, CA 91101
robert_graves@urscorp.com

[2]Department of Geological Sciences
San Diego State University
San Diego, CA 92182
day@moho.sdus.edu

submitted to: *Bull. Seismo. Soc. Am.*
March 12, 2002

Abstract

We analyze the stability and accuracy of the coarse-grain memory variable technique used for viscoelastic wave field simulations. Our analysis is an extension of the original work describing the coarse-grain methodology presented by Day (1998) and Day and Bradley (2001). Here, we show that the general behavior of the coarse-grain system is well described by effective parameters (M_E and Q_E) that are derived from the harmonic average of the moduli over the volume of the coarse-grain cell. In addition, the use of these effective parameters proves essential for analyzing the performance and accuracy of the coarse-grain system for low values (less than about 20) of Q. By analyzing the functional form of the viscoelastic modulus, we derive a necessary stability condition for the coarse-grain system, which requires that the weighting coefficients be bounded between zero and one. Specifying the weights using the approach of Day and Bradley (2001) satisfies this condition for Q values of about 3 and larger; however, using unconstrained optimization techniques will often produce weights that violate this condition at much higher Q values. We also derive an improved formulation of the original coarse-grain methodology called the element specific modulus (ESM) formulation. In the ESM formulation, each element of the coarse-grain cell uses a different unrelaxed modulus and we provide theoretical expressions for these unrelaxed moduli. We demonstrate that the accuracy of the coarse-grain system for Q values lower than about 20 is significantly increased by using the ESM formulation. Furthermore, the cost of implementing the ESM formulation is virtually identical to that of the original formulation. Finally, we present a technique for optimizing the accuracy of the coarse-grain system for very low Q values. The optimization of the coarse-grain system requires the use of the effective quality factor (Q_E), and we demonstrate that using conventional optimization techniques that do not employ the effective parameter Q_E will actually degrade the accuracy of the resulting coarse-grain system.

Introduction

The memory variable technique offers a powerful tool for the incorporation of anelasticity into time domain wave field simulations (e.g., Day and Minster, 1984; Emmerich and Korn, 1987; Carcione et al., 1988). This technique models a prescribed attenuation behavior by constructing a complex-valued modulus in the frequency domain using a linear combination of multiple relaxation mechanisms (e.g., Liu et al., 1976). Transformation into the time domain yields a set of memory variables (one for each relaxation mechanism) that are updated using first-order differential equations. Increasing the number of relaxation mechanisms will increase the applicable bandwidth of the attenuation operator and will also improve the fit to the target attenuation model. In addition, to achieve the same degree of accuracy, models with strong attenuation (low Q) will generally require more relaxation mechanisms than models with weak attenuation (high Q). The drawback with using more relaxation mechanisms in the attenuation model is the large cost increase associated with updating and storing the additional memory variables. This is particularly burdensome for 3D applications where the use of more than just one or two discrete relaxation mechanisms can be very costly (e.g., Robertsson et al., 1994; Xu and McMechan, 1998).

To address this issue, Day (1998) developed a coarse-graining methodology for memory variable calculations. In the coarse-grain approach, individual relaxation mechanisms are distributed in a spatially periodic manner across adjacent nodes of a finite-difference or finite-element grid. For 3D models, up to eight discrete relaxation mechanisms (one per grid node) can be accommodated in each coarse-grain cell. Using perturbation theory and verified by example, Day (1998) showed that the coarse-grain approach yields highly accurate results for $Q \gg 1$ as long as the wave field is sampled at a minimum of 4 points per wavelength. Furthermore, since only one relaxation mechanism is needed at each grid location, a tremendous reduction in storage and computational cost is realized. Recently, Day and Bradley (2001) have successfully extended the coarse-grain methodology to viscoelastic simulations.

The analyses of Day (1998) and Day and Bradley (2001) concentrate on the behavior of the coarse-grain system for constant (frequency independent) Q_0 values of 20 and greater. Using numerical examples, they find that the apparent Q measured from coarse-grain calculations matches the target Q_0 to within 4% tolerance over about two decades in frequency.

While the range $Q > 20$ covers many seismological applications, recent studies illustrate the potential importance of considering even lower Q values. For example, Xu and McMechan (1998) cite Q values as low as 3 for shallow seismic reflection experiments, and Olsen et al. (2001) require Q values as low as 10 for the modeling of long period (T > 2 sec) earthquake ground motions in the Los Angeles basin. Other applications using very low Q values include numerical dampers, such as sponge-zones (Israeli and Orzag, 1981) that are used to reduce artificial reflections along computational boundaries. These applications stress the need to gain a better understanding of the coarse-grain system for low Q values.

Our approach here is to develop theoretical expressions that can be used to accurately describe the performance and behavior of the coarse-grain system, especially for low values of Q. We accomplish this by using *effective* parameters (M_E and Q_E), which are derived from the harmonic average of the viscoelastic moduli over the volume of the coarse-grain cell. These theoretical expressions predict that the behavior of the coarse-grain system begins to significantly deviate from that of the general (or non-coarse-grain) system when the target Q_0 value is less than about 20. This result has important implications for analyzing the accuracy of coarse-grain calculations and for developing improved formulations of the coarse-grain system.

In the sections that follow, we first provide a brief background of the memory variable approach and the coarse-grain implementation, including the specification of the effective parameters M_E and Q_E. Next, we derive a stability condition for the coarse-grain system and present an analysis of stability thresholds for optimized and non-optimized systems. We show that optimized systems will generally violate the stability threshold at much larger Q values than the non-optimized system. This is followed by a derivation of expressions for the unrelaxed (or infinite frequency) moduli using the element specific modulus (ESM) formulation. This formulation assigns a different unrelaxed modulus to each relaxation mechanism and better represents the dispersive properties of the attenuating medium. We demonstrate through a series of example calculations that the ESM formulation provides improved accuracy relative to the conventional formulation, at virtually the same computational cost. In addition, we also show that the results of the ESM calculations are in very good agreement with the theoretical behavior of the coarse-grain system as predicted by the effective parameters M_E and Q_E. We then present a procedure for optimizing the accuracy of the

coarse-grain system based on the use of Q_E, and we show that very good results are obtained even for Q values as low as 2. We conclude with a layered model comparison to demonstrate the effectiveness of the ESM formulation in the presence of sharp media interfaces (including a free surface) and then we discuss some practical considerations of applying the coarse-grain system in generally heterogeneous 3D media.

Viscoelastic Modulus Representation

In the frequency domain, a general viscoelastic modulus $M(\omega)$ can be approximated using a discrete relaxation spectrum as

$$M(\omega) = M_u \left[1 - \frac{\delta M}{M_u} \sum_{j=1}^{N} \frac{a_j}{i\omega\tau_j + 1} \right] \quad , \tag{1}$$

where M_u is the unrelaxed modulus, $\frac{\delta M}{M_u}$ is the modulus reduction factor, τ_j are relaxation times ($\tau_j = 1/\omega_j$), a_j are coefficients chosen to fit a desired spectrum, and $i = (-1)^{1/2}$ is the imaginary unit. Equation (1) follows from either equation (25) of Day and Minster (1984) or equation (11) of Emmerich and Korn (1987). Using equation (1), the quality factor is given by

$$Q(\omega) \equiv \frac{\mathrm{Re}[M(\omega)]}{\mathrm{Im}[M(\omega)]} = \frac{1 - \frac{\delta M}{M_u} \sum_{j=1}^{N} \frac{a_j}{\omega^2\tau_j^2 + 1}}{\frac{\delta M}{M_u} \sum_{j=1}^{N} \frac{a_j \omega\tau_j}{\omega^2\tau_j^2 + 1}} \quad . \tag{2}$$

In the general application of the memory variable method, given a target $Q(\omega)$, the coefficients a_j and τ_j can be prescribed using Padé approximants (Day and Minster, 1984) or simple approximation formulas (e.g., Day and Bradley, 2001), or alternatively, equation (2) can be used to solve for the coefficients a_j and τ_j numerically (e.g., Emmerich and Korn, 1987; Xu and McMechan, 1998). Once the a_j and τ_j are set, equation (1) can be used to derive the viscoelastic wave equations and associated memory variable equations (N equations in all), which then must be solved at each computational node in the model grid

(for details, see Emmerich and Korn, 1987; Robertsson et al., 1994; Xu and McMechan, 1998).

Coarse-Grain Implementation

Without loss of generality, we can rewrite equation (1) as

$$M(\omega) = M_u \left[1 - \sum_{j=1}^{N} \frac{x_j}{i\omega\tau_j + 1} \right] \quad , \tag{3}$$

where we have set

$$x_j = \frac{\delta M}{M_u} a_j \quad . \tag{4}$$

In the coarse-grain approach, the N memory variables associated with equation (3) are distributed over N adjacent grid elements of the discrete simulation model, so that there is only one memory variable for each grid element (Day, 1998; Day and Bradley, 2001). This implies that each grid element has its own discrete viscoelastic modulus given by

$$M_k(\omega) = M_{k_u} \left[1 - \frac{\bar{x}_k}{i\omega\tau_k + 1} \right] \quad , \tag{5}$$

where $k = 1, \cdots, N$ in the periodic manner described by Day (1998), M_{k_u} is the element specific unrelaxed modulus, and

$$\bar{x}_k = \frac{V_T}{V_k} x_k \tag{6}$$

are the volumetric normalized coefficients, with the volume of the k^{th} grid element given by V_k and the total volume of the N adjacent grid elements given by $V_T = \sum_{j=1}^{N} V_j$.

The coarse-grain theory developed by Day (1998) states that for wavelengths longer than about 4 grid elements and for $Q \gg 1$, the application of equation (5) at N adjacent

grid elements will yield a good approximation to the general relaxation spectrum given by equation (1), and thus will also satisfactorily reproduce the attenuation behavior predicted by equation (2).

However, as will be shown later, the general behavior of the coarse-grain system is actually better described not by the general modulus given in equation (1), but rather by the *effective* modulus that is derived from the harmonic average of the $M_k(\omega)$ over the volume of the coarse-grain cell. We define this effective modulus as $M_E(\omega)$, which is given by

$$M_E(\omega) = V_T\Big[\sum_{k=1}^{N} \frac{V_k}{M_k(\omega)}\Big]^{-1} \quad , \tag{7}$$

with an associated effective quality factor $Q_E(\omega)$ given by

$$Q_E(\omega) = \frac{\mathrm{Re}[M_E(\omega)]}{\mathrm{Im}[M_E(\omega)]} \quad . \tag{8}$$

More complete expressions for $M_E(\omega)$ and $Q_E(\omega)$ are given in the Appendix. Our use of harmonic averaging to define effective parameters follows from analogous formulations used to precisely represent media heterogeneity in grid based calculations (e.g., Zahradník et al., 1993; Graves, 1996; Moczo et al., 2001). In the next section, we show that for target Q values greater than about 20, there is little difference between the effective modulus given by equation (7) and the general modulus given by equation (1). However, for smaller values of Q, the difference becomes quite significant, and it is shown that the behavior of the coarse-grain system follows very closely the theoretical behavior predicted by these effective parameters. Thus, these effective parameters provide a general framework for analyzing and optimizing the accuracy of the coarse-grain system, particularly for low values of Q.

Stability Analysis

In order to ensure physical stability for any viscoelastic modulus, two necessary conditions must be satisfied. First, the modulus at zero frequency (relaxed modulus) must remain strictly positive, and second, the general viscoelastic modulus must be dissipative

for all frequencies. The first condition above follows from thermodynamic considerations of Hooke's law, and the second condition places a positivity constraint on the quality factor (negative values would give rise to energy amplification, not dissipation). Satisfying both of these conditions using the discrete relaxation spectrum formulation requires that both the real and imaginary parts of the spectrum remain positive.

Starting with equation (5), we rewrite this expression into its discrete real and imaginary parts, giving

$$M_k(\omega) = M_{k_u}\left[1 - \frac{\bar{x}_k}{\omega^2\tau_k^2 + 1} + i\frac{\bar{x}_k\omega\tau_k}{\omega^2\tau_k^2 + 1}\right] \quad . \tag{9}$$

Visual inspection of equation (9) leads to the following stability condition

$$0 \leq \frac{\bar{x}_k}{\omega^2\tau_k^2 + 1} < 1 \quad , \tag{10}$$

which, since this must hold for all $\omega^2 \geq 0$, can be simplified to

$$0 \leq \bar{x}_k < 1 \quad . \tag{11}$$

Equation (11) represents a necessary stability condition for the memory variable system, thus it must be satisfied regardless of how the $\bar{x}_k$ and τ_k coefficients are determined.

In satisfying this stability condition, there exists a tradeoff between the absorption bandwidth over which the prescribed relaxation spectrum is valid and the accuracy to which this relaxation spectrum matches the desired Q model. Furthermore, given a prescribed absorption bandwidth, there will generally be some minimum value of the desired Q model below which the stability condition will be violated. For example, Day (1998) and Day and Bradley (2001) assume a frequency independent Q model and use a simple procedure to set all of the coefficients $\bar{x}_k$ in the coarse-grain system equal to the same constant value

$$\bar{x}_k = \frac{\delta M}{M_u} \approx \frac{2\ln(\tau_M/\tau_0)}{\left[\pi Q_0 - 2\ln(\omega_0\tau_0)\right]} \quad , \tag{12}$$

with the τ_k evenly distributed on a logarithmic scale

$$\ln \tau_k = \ln \tau_0 + \frac{2k-1}{2N}\Big[\ln(\tau_M/\tau_0)\Big] \qquad k = 1, \cdots, N \quad . \tag{13}$$

Here, τ_0 and τ_M are the lower and upper absorption-band cutoffs, and ω_0 is a prescribed reference frequency where the resulting relaxation spectrum matches the desired constant Q_0. Setting $\omega_0 = (\tau_M \tau_0)^{-1/2}$ (i.e., the geometric average of the absorption-band cutoffs), inserting equation (12) into the stability condition (11) and rearranging terms, we get

$$-\pi Q_0 \leq \ln(\tau_M/\tau_0) < \pi Q_0 \quad . \tag{14}$$

By definition $\tau_M > \tau_0$, thus the lower bound condition will always be satisfied with this simple parameterization. However, for a given τ_M and τ_0, there will always be a minimum (positive) Q_0 below which the upper bound condition will be violated. For example, using numerical experiments, Day (1998) showed that the relation $\tau_M/\tau_0 = 10^4$ provides a nearly frequency independent Q (for $Q \geq 20$) over more than two decades of bandwidth. Inserting this value into equation (10), we have the requirement $Q_0 > \ln(10^4)/\pi \approx 3$.

Figure 1 plots the resulting $Q(\omega)$ and $Q_E(\omega)$ obtained from equations (2) and (A6), Figure 1 respectively, using the above coefficient parameterization [i.e., equations (12) and (13)] with $N = 8$, and various target values of Q_0. Also shown on this plot are the values of $\bar{x}_k$ associated with each Q_0. This plot clearly shows that as the target Q_0 decreases, the approximation provided by the above parameterization becomes increasingly less accurate. In addition, as Q_0 decreases, the $\bar{x}_k$ coefficients increase, with the value at $Q_0 = 2$ exceeding the stability limit. This figure also shows that the effective quality factor $Q_E(\omega)$ provides a less accurate fit to the target Q_0 than the general quality factor $Q(\omega)$ that would result from a non-coarse-grain implementation. For this parameterization, the difference between $Q(\omega)$ and $Q_E(\omega)$ is only significant for Q_0 less than about 10. Numerical simulations are in agreement with this theoretical behavior.

In theory, more accurate representations of $Q(\omega)$ can be obtained by optimizing the $\bar{x}_k$ and τ_k using numerical techniques (e.g., Emmerich and Korn, 1987; Xu and McMechan,

1998). Although these optimization procedures can provide a very accurate match to the general $Q(\omega)$ over a specified bandwidth, they will generally produce $\bar{x}_k$ that will violate the coarse-grain stability condition (11) at a much higher target Q value than when using a simpler approximation. Furthermore, the effective quality factor of the coarse-grain system $Q_E(\omega)$ obtained from these types of optimization procedures can be very different from the general $Q(\omega)$.

We demonstrate this behavior by using the least-squares algorithm of Emmerich and Korn (1987) to solve for the coefficients $\bar{x}_k$ for various values of Q_0. Again, the τ_k were prescribed using the relation of Day and Bradley (2001) and we set $\tau_M/\tau_0 = 10^4$ and $N = 8$. Figure 2 plots the resulting $Q(\omega)$ and $Q_E(\omega)$ for this parameterization, and various values of Q_0. Also shown are the maximum of the $\bar{x}_k$ coefficients obtained for each Q_0. Clearly, the match to the general attenuation model $Q(\omega)$ is quite accurate even for very small values of Q_0. However, the maximum of the $\bar{x}_k$ coefficients increases quite rapidly with decreasing Q_0, and exceed the stability limit at about $Q_0 = 10$. In addition, as Q_0 decreases, the effective quality factor $Q_E(\omega)$ begins to diverge quite significantly from the general $Q(\omega)$. Since it is the $Q_E(\omega)$ that governs the attenuation behavior of the coarse-grain method, optimizing the fit to the general $Q(\omega)$ will actually degrade the accuracy of the coarse-grain system. This behavior will be demonstrated later by example, and we will subsequently exploit this fact to show that improved accuracy can be obtained by optimizing directly on $Q_E(\omega)$ instead of on $Q(\omega)$.

Figur

Specification of the Element Specific Unrelaxed Modulus

Day and Bradley (2001) give an expression for the unrelaxed modulus based on the constant Q_0 model, and they assume that the unrelaxed modulus (M_u) is the same at all of the N adjacent grid elements in the coarse-grain system. For Q_0 greater than about 20, this approach works reasonably well. However, this formulation equalizes the element specific phase velocities at infinite frequency. Since each relaxation mechanism gives rise to a different dispersion relation, the result is to induce small-scale heterogeneity in the phase velocity at those frequencies that fall within or below the absorption band. The performance of the method is improved, especially at very low Q, if we instead minimize the phase velocity heterogeneity at some reference frequency falling near the center of the

band of computational interest. We can accomplish this by permitting the element specific unrelaxed moduli (M_{k_u}) to vary within the coarse-grain cell in such a way as to equalize the element specific frequency-dependent moduli at the reference frequency. Here, we derive an expression for such an element specific unrelaxed modulus.

Following Kjartansson (1979), the phase velocity in an attenuating medium is given by

$$c^{-1}(\omega) = \mathrm{Re}\left[\left(\frac{\rho}{M(\omega)}\right)^{1/2}\right] \quad , \tag{15}$$

where ρ is the medium density. Inserting the element specific modulus [equation (9)] for the modulus in equation (15), and then evaluating the resulting expression at a reference frequency $f_0 = \omega_0/2\pi$, we get (after rearranging terms)

$$M_{k_u} = c_0^2 \, \rho \, \frac{1}{2}\left[A_{k_0}^2 + B_{k_0}^2\right]^{-1/2}\left\{1 + A_{k_0}\left[A_{k_0}^2 + B_{k_0}^2\right]^{-1/2}\right\} \quad , \tag{16}$$

where

$$A_{k_0} = 1 - \frac{\bar{x}_k}{\omega_0^2\tau_k^2 + 1} \qquad \text{and} \qquad B_{k_0} = \frac{\bar{x}_k\omega\tau_k}{\omega_0^2\tau_k^2 + 1} \quad , \tag{17}$$

and c_0 is the prescribed propagation velocity at the reference frequency.

Equation (16) can be interpreted as a prescription for a set of element specific unrelaxed moduli M_{k_u} that ensure spatial homogeneity (i.e., over the coarse-grain cell) of the modulus at the reference frequency f_0. This equation has two important implications. First, even if the reference medium is entirely homogeneous, this expression requires that the N adjacent grid elements in the coarse-grain system each have a different elastic (unrelaxed) modulus. However, this apparent heterogeneity will only exist at very short wavelengths (and high frequencies). The above parameterization will provide a good approximation to the frequency dependent modulus as long as the propagation wavelengths are about 4 grid elements or greater [consistent with the coarse-grain theory developed by Day (1998)]. For low-order FD and FE implementations, this condition is easily satisfied.

The second implication of using equation (16) is that the maximum allowable time step will be controlled by the largest M_{k_u} in the entire model domain, which will always be larger than the corresponding effective M_u. This effect might be significant, particularly when low values of Q_0 occur in the highest velocity portions of the model. Fortunately, the lowest Q values tend to strongly correlate with the lowest velocities, so the overall impact of this second effect is generally not significant.

In order to demonstrate the importance of using the element specific modulus given by equation (16), we have performed a series of numerical calculations using a 3D staggered-grid finite difference code (Graves, 1996). These calculations use plane wave models similar to that used by Day (1998) and Day and Bradley (2001). The calculations are initiated by imposing a velocity pulse with shape $s(t) = t\exp(-t/T)$ along one plane of the 3D grid. Motion is specified either normal (P wave) or parallel (S wave) to the plane. The medium is homogeneous with P and S wave velocities of 6 km/s and 3.46 km/s, respectively, prescribed at a reference frequency $f_0 = 1$ Hz, and a density of 2.7 g/cm^3.

We use a constant Q model and set the $\bar{x}_k$ and τ_k coefficients using equations (12) and (13). Two values of Q_0 are considered, 20 and 5, and the associated τ_0, τ_M, f_0 and c_{max} [maximum propagation velocity as determined from equation (16)], are shown in Table 1. Table 1
These values of τ_0 and τ_M give a target bandwidth for the constant Q_0 model of about four decades (roughly 0.01 Hz to 100 Hz). For all calculations, the source duration parameter T is set to 0.1 and the grid spacing is 0.1 km.

Figure 3 plots the velocity waveforms simulated at a propagation distance of 10 km Figure 3
for each of the above cases. The analytic solution is computed using the formulation of Kjartansson (1979). We used two different formulations to specify the unrelaxed modulus in the FD simulations. The first (labeled *"Element Specific M_{k_u}"* and hereafter referred to as the ESM formulation) uses equation (16) to determine the element specific unrelaxed modulus for each of the 8 adjacent grid elements in the coarse-grain system. The second (label *"Constant M_u"*, and hereafter referred to as the CM formulation) uses the method of Day and Bradley (2001) to determine a single unrelaxed modulus, which is then used for all grid elements in the entire model. For all cases, the velocity pulse is normalized to unit amplitude at zero distance.

For $Q_0 = 20$, the ESM formulation gives an excellent match to the timing, waveform and amplitude of the analytic time history for both P and S waves. The CM formulation produces a very good result for this Q_0 value as well, with the only noticeable shortcoming being a slight phase delay of the pulse. At $Q_0 = 5$, the difference in performance between the two formulations is much more significant, with the ESM formulation clearly providing a better overall match to the analytic response. Although both formulations underpredict the amplitude of the analytic pulse, the CM response also exhibits a significant phase delay.

Taking the response at two locations separated by a distance Δx, we can measure the apparent Q from these plane wave tests using the relation

$$Q_A^{-1}(\omega) = -2 \frac{c(\omega)}{\omega \Delta x} \left[\ln \left| v(x + \Delta x, \omega) \right| - \ln \left| v(x, \omega) \right| \right] \quad , \tag{18}$$

where $|v(x,\omega)|$ is the Fourier amplitude spectrum of the velocity time history at location x and the frequency dependent phase velocity $c(\omega)$ is given by (Kjartansson, 1979)

$$c(\omega) = c_0 \left| \frac{\omega}{\omega_0} \right|^{\gamma} \left[\cos\left(\frac{\pi\gamma}{2}\right) \right]^{-1} \quad , \tag{19}$$

with c_0 the specified velocity at reference frequency f_0 and

$$\gamma = \frac{1}{\pi} \tan^{-1} \left[\frac{1}{Q_0} \right] \quad . \tag{20}$$

Equation (18) differs slightly from the relation used by Day and Bradley (2001) in that we use $c(\omega)$ instead of the constant c_0. The form used here gives more accurate results for low Q values.

Figure 4 plots the Q_A computed for each of the above plane wave calculations at a separation distance of $\Delta x = 2$ km. These results are plotted up to 12 Hz for P waves and 7 Hz for S waves, which corresponds to a sampling of 5 grid points per respective wavelength. The low frequency cutoff for the results is determined by the total computed duration, which is generally about 12-15 seconds.

Figure 4

For $Q_0 = 20$, both formulations do reasonably well at matching the desired Q behavior over roughly two decades of frequency (centered at the reference value of 1 Hz). As discussed by Day (1998) and demonstrated by the results in Figure 4, the accuracy of the coarse-grain method begins to diminish near the 5 grid points per wavelength sampling limit. For $Q_0 = 5$, the accuracy of both formulations is reduced relative to the higher Q_o case. However, the ESM formulation still matches the target Q_0 value to about $\pm 25\%$ over the central two decade frequency band, whereas the CM formulation significantly underpredicts the target Q_0 over most of this same bandwidth.

Also shown in the panels of Figure 4 are the coarse-grain effective Q curves $[Q_E(\omega)]$ given by equation (A6). In each case, the ESM formulation follows the theoretical behavior of the $Q_E(\omega)$ curve reasonably well, particularly for frequencies above 1 Hz. At lower frequencies, the ESM results deviate somewhat from the theoretical curves (most noticeable for the S wave case at low Q). We suspect that this deviation is caused by (very low amplitude) artificial boundary reflections, which are virtually impossible to suppress competely from the calculations. The importance of considering the $Q_E(\omega)$ behavior will be discussed further in the following section.

As a final comparison, we have computed the P and S wave phase velocities for each of the plane wave calculations, and these results are plotted in Figure 5. The phase velocity Figure 5
is obtained by measuring the phase delay of each Fourier component in the computed time history at two adjacent locations (1 km apart in this case). In the plots shown in Figure 5, we have normalized the measured phase velocity by the theoretical value given by equation (19), thus a value of one gives an exact match to the analytic result.

For $Q_0 = 20$, the ESM formulation provides a very close match to the theoretical result across roughly two decades of frequency. The CSM formulation produces a phase velocity which is about 1% less than the theoretical value over this same bandwidth. This result is consistent with the observed phase delay seen in Figure 3. For $Q_0 = 5$, both formulations exhibit significant dispersion relative to the theoretical value; however, the ESM formulation clearly provides a more accurate result. The largest mismatch of the ESM formulation is on the order of a few percent and occurs at the lower frequencies. In the time domain, this is manifest by a slight delay of the waveform tails as seen in the lower panels of Figure 3. On

the other hand, the CM formulation underpredicts the theoretical value by roughly 10% over most of the bandwidth, resulting in a noticeable delay of the entire waveform pulse as shown in Figure 3. Also shown in this figure are the effective phase velocity curves $c_E(\omega)$, which we have derived from the effective modulus $M_E(\omega)$ using equation (15). For each case, the behavior of the ESM calculation is predicted nicely using the theoretical $c_E(\omega)$ curves.

Significance of Effective Parameters M_E and Q_E

The importance of using the effective parameters M_E and Q_E to analyze the behavior of the coarse-grain system is further demonstrated by the results shown Figure 6. Here, we approximate a constant Q_0 of 12 with the general $Q(\omega)$ given by equation (2) and solve for the $\bar{x}_k$ coefficients using the least-squares algorithm of Emmerich and Korn (1987). The τ_k are the same as in the preceding calculations, and we use the ESM formulation. As shown in Figure 2, this parameterization gives a maximum $\bar{x}_k$ that is just within the stability threshold for the coarse-grain system. Figure 6 compares the theoretical and computed waveforms, apparent attenuation (Q_A), and measured phase velocity for this formulation. In the following, we show results for P waves, although very similar results are obtained for S waves.

Figure 6

As discussed earlier (Figure 2), the theoretical behavior of the general $Q(\omega)$ for this formulation matches the constant Q_0 of 12 very well over nearly 4 decades of frequency. However, the comparisons in Figure 6 clearly demonstrate that the resulting behavior of the coarse-grain calculation is actually predicted much more closely by the effective parameters, $Q_E(\omega)$ and $c_E(\omega)$ [derived from $M_E(\omega)$ using equation (15)]. Furthermore, these results also demonstrate that using the general $Q(\omega)$ to determine the choice of the $\bar{x}_k$ coefficients for the coarse-grain system actually results in a significant degradation in the accuracy of the calculation.

Improved Accuracy and Stability for Low Q_0

The results from the preceding section suggest that a better approach for improving the accuracy of the coarse-grain system is to use the effective parameter $Q_E(\omega)$ instead of the general $Q(\omega)$ to guide the determination of the $\bar{x}_k$ and τ_k coefficients (e.g., by optimizing the fit to the target Q_0).

The relationship among the $\bar{x}_k$, τ_k and $Q_E(\omega)$ is highly non-linear (see Appendix). Here, we use a simple grid search perturbation algorithm to determine the coefficients given a target Q_0. In general, any of a variety of non-linear solution algorithms can be used to determine these coefficients, each having its own optimization criteria. Our fitting criterion seeks to minimize the sum of the squared residuals between $Q_E(\omega)$ and Q_0 over the prescribed absorption bandwidth. The approach used here results in a system which matches the target Q_0 reasonably well over about two decades in frequency (as shown below). Table 2 lists the coefficients for target Q_0 values of 5 and 2 determined with this technique for the ESM formulation. Figures 7, 8 and 9 show, respectively, the waveforms, apparent attenuation (Q_A) and phase velocity obtained from plane P and S wave calculations which use these optimized parameters. All other model parameters are the same as in previous tests.

For $Q_0 = 5$, an excellent fit is obtained between the theoretical and computed responses, with the measured Q_A matching the target Q_0 to within a few percent over roughly two decades of frequency. In Figures 8 and 9, we also show theoretical curves for $Q_E(\omega)$ and $c_E(\omega)$ to illustrate how the computed response closely follows the behavior predicted by the effective parameters. For $Q_0 = 2$, the fit to the theoretical response is still remarkably good, with the measured Q_A matching the target Q_0 to within a few percent over roughly one-and-a-half decades of frequency. Again, the effective parameters $Q_E(\omega)$ and $c_E(\omega)$ provide a reasonably accurate prediction of the behavior of the computed results.

It becomes increasingly difficult to derive a coarse-grain system that is valid over an appreciable bandwidth for Q values lower than about 2 because the $\bar{x}_k$ coefficients are very close to the stability limit (see Table 2). The only way to maintain stability for these very low Q values is to decrease the spread of the τ_k coefficients. In the limit that all the τ_k are equal, the coarse-grain system reduces to a narrow-band model with only a single memory variable (Robertsson et al., 1994).

Layered Model Test

We test the performance of the coarse-grain formulations in more complex media (including a free surface) by running calculations for the three layer model listed in Table 3. A point double-couple with strike = 90°, dip = 90°, rake = 0° and $M_0 = 10^{23}$ dyne · cm is

used to initiate the calculations. The source depth is 2 km and the moment rate function is a cosine-bell function given by

$$\dot{M}_0(t) = \begin{cases} \frac{M_0}{T}(1 - \cos 2\pi t/T), & \text{if } 0 \le t \le T; \\ 0, & \text{otherwise;} \end{cases} \tag{21}$$

with a width of $T = 0.2$ s. The resulting time histories are analyzed for an observation point located 5 km from the source at an azimuth of 143°. The FD calculations use a grid spacing of 100 m, yielding a maximum frequency resolution of 1 Hz for a shear wave sampling of 5 grid points per wavelength in the lowest velocity region of the model. In addition to the finite difference (FD) calculations, we also compute the solution using the frequency wavenumber (FK) technique. All results are low-pass filtered using a fourth-order, zero-phase Butterworth operator with a corner at 1 Hz.

First we compare the FD and FK results for a purely elastic (infinite Q) model. This comparison allows us to analyze the fidelity of the FD solution for the prescribed model parameters. Figure 10 plots the computed time histories and their associated Fourier amplitude spectra. The agreement between the FD and FK results is excellent in both the time and frequency domains. The only noticeable difference is a very slight delay of some of the later phases of the FD result, which can be attributed to the effects of numerical grid dispersion within the shallowest velocity layer. Figure 10

Figure 11 compares the three coarse-grain FD formulations (Optimized ESM, ESM and CM) with the FK result for the anelastic model. Obviously, the effects of anelasticity have a strong impact on the waveforms relative to the purely elastic case, most notably by reducing the overall amplitude of the signals and by suppressing much of the later arriving, shorter period energy. Both the Optimized ESM and ESM formulations do an excellent job of matching the waveforms and spectra of the anelastic FK result, demonstrating the ability of these formulations to accurately model very low (spatially variable) Q in the presence of sharp media boundaries and a free surface. In addition, the CM formulation performs reasonably well for this model. However this formulation tends to underpredict the amplitudes of the waveforms (particularly at shorter periods on the horizontal components), and also exhibits a Figure 11

noticeable phase delay of the S waves and surface waves. These characteristics are consistent with the theoretical behavior of the CM formulation as discussed earlier.

Discussion

The examples and theoretical analysis in the previous sections demonstrate the improved accuracy that is provided by the ESM formulation compared to the CM formulation, particularly for low Q values. From a practical standpoint, the implementation cost of the ESM formulation is virtually identical to the CM formulation (about 50% - 60% increase in memory and CPU for either formulation relative to the purely elastic case). The one possible exception to this would be a model where the highest velocity material also had a very low Q, in which case the ESM formulation would require a smaller time step than the CM formulation. Fortunately, for most applications the lowest Q values tend to strongly correlate with the lowest velocities, so the impact of this effect will generally be insignificant. In fact, for our layered model test, the time step requirement was the same for the CM, ESM and Optimized ESM formulations.

Our results also demonstrate that the Optimized ESM formulation can provide a high degree of accuracy for very low Q models. However, there are some issues concerning the general application of the optimized formulation that warrant further discussion. First, the overhead cost associated with determining the optimized $\bar{x}_k$ and τ_k coefficients for a generally heterogeneous 3D model may be quite significant. For example, Olsen et al. (2001) have proposed a Q model for the LA basin that is proportional to the local seismic wave velocity, which may be different at each grid point in the model. Optimization would require the calculation of the coefficients at each coarse-grain cell having a different Q_p and/or Q_s value. Some cost savings may be realized by precomputing and tabulating the coefficients for a a limited number of reference Q values, and then assigning a reference value to each grid point. However, the practical benefit and accuracy of this type of approach needs further investigation.

An additional issue involves the trade-off between the added cost of optimization and the benefit of increased accuracy. Our layered model test indicates that there is not a significant difference in the performance of the optimized versus non-optimized versions of

the ESM formulation even for models with Q values as low as 5. Most seismic applications fall into a class of models with $Q > 5$, and our results suggest that the non-optimized ESM formulation can easily handle these applications with a very high degree of accuracy. For models with $Q < 5$ (e.g., shallow reflection applications; Xu and McMechan, 1998), optimized formulations may be used, or alternatively, the non-optimized ESM formulation can also be extended to very low Q values by reducing the range of the absorption band [see equation (14)].

Another potential application involving very low Q is the suppression of artificial reflections in sponge-zones adjacent to absorbing boundaries (Israeli and Orzag, 1981; Robertsson et al., 1994). The broadband nature of the coarse-grain system allows for a more complete absorption of energy than the single memory variable scheme proposed by Robertsson et al. (1994) at no additional cost. For efficiency, we use the CM formulation in the sponge-zone and gradually reduce the Q values to a minimum of $Q = 5$ right at the boundary. Although the CM formulation is less accurate than the ESM formulation, it requires a smaller value of the unrelaxed modulus, which consequently permits a larger time step. This is an important consideration when high velocity regions of the model lie along the computational boundary. The loss of accuracy in the sponge-zone is of no practical significance since the goal is to remove this energy from the system anyway.

As a final point of discussion, we note that while most of the theoretical analysis presented here is based on simple models, our ultimate goal is to apply this technique to generally heterogeneous 3D media. In this case, each grid element may have different moduli and Q values. However, with the coarse-grain method, all elements of the coarse-grain cell (eight adjacent nodes in 3D) must have the same Q value (although they can still have different moduli). This effectively limits the spatial resolution of Q variability to twice the grid size. Previous studies have shown that harmonic averaging of the volumetrically normalized moduli provides the correct representation of internal media boundaries, even at the sub-grid level (e.g., Zahradník et al., 1993; Graves, 1996; Moczo et al., 2001). Following this approach, we calculate the target Q value for each coarse-grain cell by harmonically averaging the eight input Q values over the volume of the coarse-grain cell. This approach has worked very well in our test calculations (e.g. the layered model test); however, further evaluation is needed to more fully document the theoretical basis for this representation.

Conclusions

In this paper, we provide a theoretical analysis of the stability and accuracy of the coarse-grain anelastic technique originally developed by Day (1998) and Day and Bradley (2001). We show that the behavior of the coarse-grain system is best described by effective parameters (M_E and Q_E) that are derived from the harmonic average of the moduli over the volume of the coarse-grain cell. The use of these effective parameters is essential for analyzing the performance and accuracy of the coarse-grain system, particularly for low values of Q. Our analysis derives a necessary stability condition for the coarse-grain system, which states that the weighting coefficients must lie between zero and one. Using the approach of Day and Bradley (2001) to specify the weights satisfies this stability condition for Q values of about 3 and larger. However, using unconstrained optimization techniques will produce weights that violate this condition at much higher Q values. We also derive a modification of the original coarse-grain methodology called the element specific modulus (ESM) formulation, in which each element of the coarse-grain cell has a different unrelaxed modulus. We demonstrate that the accuracy of the coarse-grain system for Q values lower than about 20 is significantly improved by using the ESM formulation. The cost of implementing the ESM formulation is virtually identical to the original Day and Bradley (2001) formulation. Finally, we present technique for optimizing the accuracy of the coarse-grain system for very low Q models, based on matching the effective quality factor (Q_E). In addition, we demonstrate that using optimization techniques that do not employ the effective parameter Q_E will actually degrade (rather than improve) the accuracy of the resulting coarse-grain system.

Acknowledgements

Several of the figures for the manuscript were prepared using GMT software (Wessel and Smith, 1991). This work was sponsored in part by USGS external program grant 00-HQ-GR-0060 and funding from the Southern California Earthquake Center (SCEC). SCEC is funded by NSF Cooperative Agreement EAR-8920136 and USGS Cooperative Agreements 14-08-0001-A0899 and 1434-HQ-97AG01718. The SCEC contribution number for this paper is 659.

References

Carcione, J. M., D. Kosloff, and R. Kosloff (1988). Wave propagation in a linear viscoacoustic medium, *Geophys. J. R. Astr. Soc.*, **93**, 393-407.

Day, S. M. (1998). Efficient simulation of constant Q using coarse-grained memory variables, *Bull. Seism. Soc. Am.*, **68**, 1051-1062.

Day, S. M. and C. R. Bradley (2001). Memory efficient simulation of anelastic wave propagation, *Bull. Seism. Soc. Am.*, **91**, 520-531.

Day, S. M. and J. B. Minster (1984). Numerical simulation of attenuated wavefields using a Padé approximant method, *Geophys. J. R. Astr. Soc.*, **78**, 105-118.

Graves, R. W. (1996). Simulating seismic wave propagation in 3D elastic media using staggered grid finite differences, *Bull. Seism. Soc. Am.*, **86**, 1091-1106.

Emmerich, H. and M. Korn (1987). Incorporation of attenuation into time domain computations of seismic wave fields, *Geophysics*, **52**, 1252-1264.

Israeli, M., and S. A. Orzag (1981). Approximation of radiating boundary conditions, *J. Comput. Phys.*, **41**, 115-135.

Kjartansson, E. (1979). Constant Q wave propagation and attenuation, *J. Geophys. Res.*, **84**, 4737-4748.

Liu, R., D. L. Anderson and H. Kanimori (1976). Velocity dispersion due to anelasticity: implication for seismology and mantle composition, *Geophys. J. R. Astr. Soc.*, **47**, 41-58.

Moczo, P., J. Kristek, M. Kristekova, and R. J. Archuleta (2001). Accuracy of the 3D finite-difference modeling of earthquake ground motion for real sites, *Eos. Trans. AGU*, **82**(47), Fall Meet. Suppl., Abstract S32D-10.

Olsen, K. B., C. R. Bradley and S. M. Day (2001). Estimation of Q and near surface amplification for long-period waves in the Los Angeles basin, *Seism.. Res. Lett.*, **72**, Ann. Meet. Abstract, p. 283.

Robertsson, J. O. A., J. O. Blanch and W. W. Symes (1994). Viscoelastic finite-difference modeling, *Geophysics*, **59**, 1444-1456.

Wessel, P., and W. H. F. Smith (1991). Free software helps map and display data, *Eos. Trans. AGU***72**, *441*, 445-446.

Xu, T. and G. A. McMechan (1998). Efficient 3D viscoelastic modeling with application to near-surface land seismic data, *Geophysics*, **63**, 601-612.

Zahradník , J., P. Moczo, and F. Hron (1993). Testing four elastic finite-difference schemes for behavior at discontinuities, *Bull. Seism. Soc. Am.*, **83**, 107-129.

Appendix: Complete Expressions for M_E and Q_E

From equations (7) and (9) we can write

$$M_E(\omega) = V_T \left\{ \sum_{k=1}^{N} \frac{V_k}{M_{k_u}} \left[1 - \frac{\bar{x}_k}{\omega^2 \tau_k^2 + 1} + i \frac{\bar{x}_k \omega \tau_k}{\omega^2 \tau_k^2 + 1} \right]^{-1} \right\}^{-1} , \tag{A1}$$

where the element specific unrelaxed modulus M_{k_u} is given by equations (16) and (17). Letting

$$\alpha_k = 1 - \frac{\bar{x}_k}{\omega^2 \tau_k^2 + 1} \qquad \text{and} \qquad \beta_k = \frac{\bar{x}_k \omega \tau_k}{\omega^2 \tau_k^2 + 1} , \tag{A2}$$

equation (A1) can be written as

$$M_E(\omega) = V_T \left\{ \sum_{k=1}^{N} \frac{V_k}{M_{k_u}} \left[\frac{\alpha_k}{\alpha_k^2 + \beta_k^2} - i \frac{\beta_k}{\alpha_k^2 + \beta_k^2} \right] \right\}^{-1} . \tag{A3}$$

Now setting

$$A = \sum_{k=1}^{N} \frac{V_k}{M_{k_u}} \left[\frac{\alpha_k}{\alpha_k^2 + \beta_k^2} \right] \qquad \text{and} \qquad B = \sum_{k=1}^{N} \frac{V_k}{M_{k_u}} \left[\frac{\beta_k}{\alpha_k^2 + \beta_k^2} \right] , \tag{A4}$$

we obtain the expression

$$M_E(\omega) = V_T \left[\frac{A}{A^2 + B^2} + i \frac{B}{A^2 + B^2} \right] . \tag{A5}$$

Finally, from equations (8), (A4) and (A5), we have for the effective quality factor

$$Q_E(\omega) = \frac{\sum_{k=1}^{N} \frac{V_k}{M_{k_u}} \left[\frac{\alpha_k}{\alpha_k^2 + \beta_k^2} \right]}{\sum_{k=1}^{N} \frac{V_k}{M_{k_u}} \left[\frac{\beta_k}{\alpha_k^2 + \beta_k^2} \right]} . \tag{A6}$$

TABLE 1: Attenuation parameters for plane wave tests.

Q_o	τ_o	τ_M	f_o(Hz)	c_{max}(km/s)
20	0.00159	15.9	1.0	6.97
5	0.00159	15.9	1.0	11.87

TABLE 2: Coefficients for optimized low Q_0 models.

	$Q_o = 5$		$Q_o = 2$	
k	$\bar{x}_k$	τ_k	$\bar{x}_k$	τ_k
1	0.700552	5.03655×10^{-3}	0.863550	4.48560×10^{-3}
2	0.666418	6.52579×10^{-3}	0.863550	4.48560×10^{-3}
3	0.609150	1.54751×10^{-2}	0.863550	4.48560×10^{-3}
4	0.602998	4.36147×10^{-2}	0.863550	1.78575×10^{-2}
5	0.567881	9.48709×10^{-2}	0.863550	1.78575×10^{-2}
6	0.609272	0.267383	0.863550	7.10919×10^{-2}
7	0.666418	0.753587	0.863550	0.224812
8	0.659820	1.94820	0.863550	0.252244

TABLE 3: Layered velocity structure.

V_p(km/s)	V_s(km/s)	density(g/cm^3)	Q_p	Q_s	thickness(km)
1.7	0.5	2.1	10	5	0.55
3.0	1.2	2.3	20	10	1.00
6.0	3.464	2.7	100	50	–

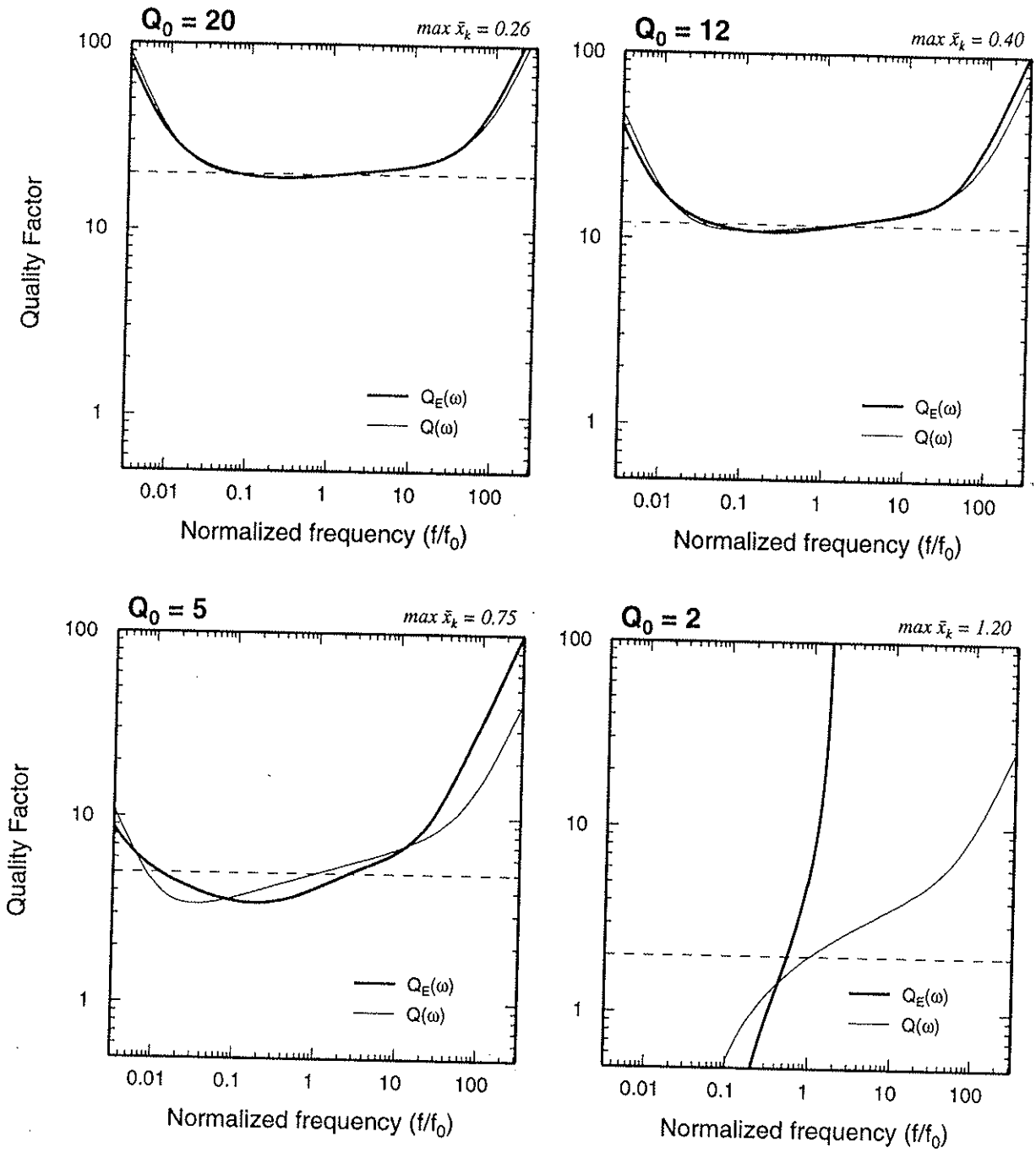

Figure 3: Plots of $Q(\omega)$ [thin line, from equation (2)] and $Q_E(\omega)$ [thick line, from equation (A6)] determined using the formulation of Day and Bradley (2001) to specify the $\bar{x}_k$ coefficients for various target values of Q_0. The maximum $\bar{x}_k$ for each Q_0 is shown at the upper right of each panel.

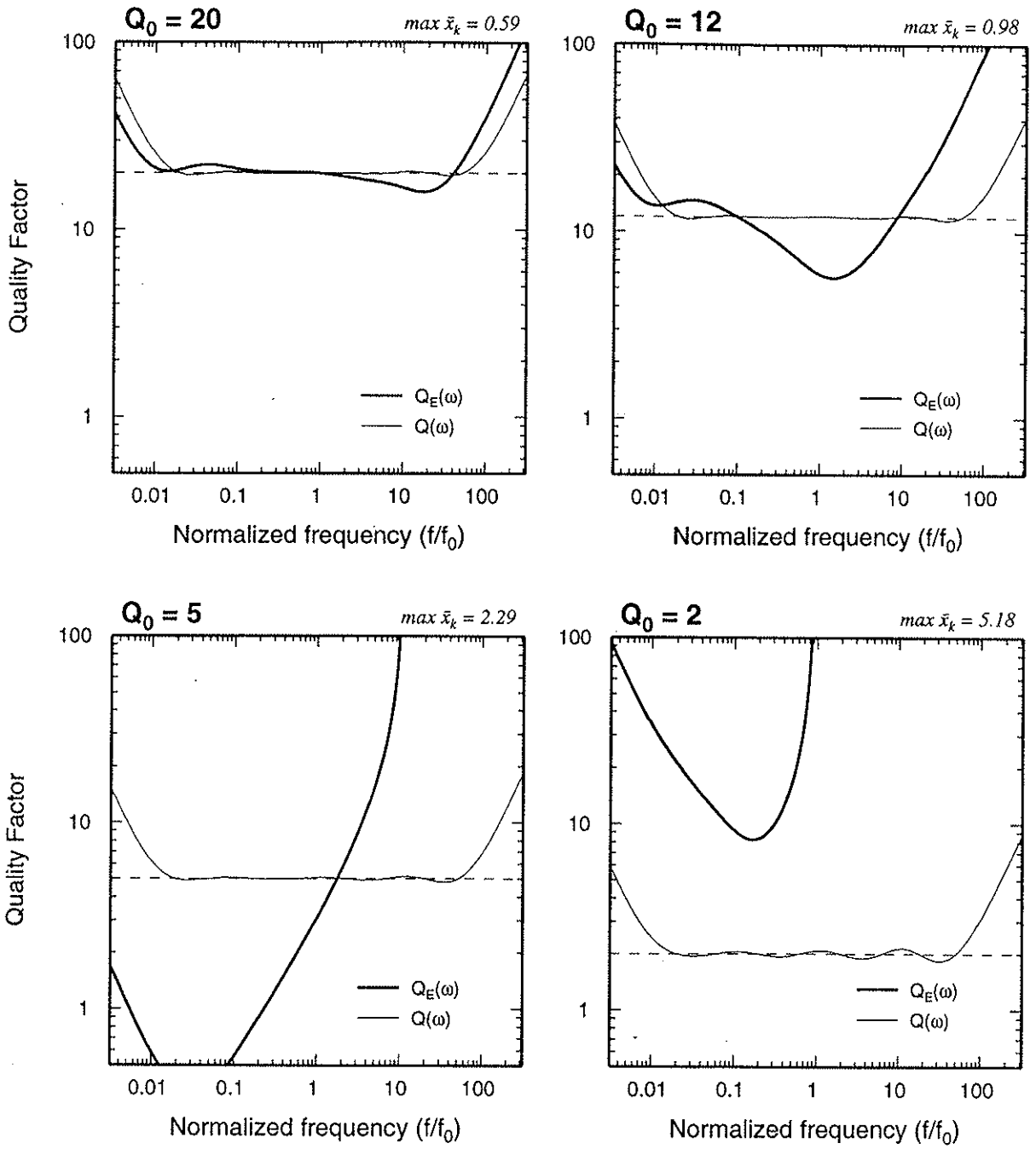

Figure 4: Plots of $Q(\omega)$ [thin line, from equation (2)] and $Q_E(\omega)$ [thick line, from equation (A6)] determined using the least-squares formulation of Emmerich and Korn (1987) to specify the $\bar{x}_k$ coefficients for various target values of Q_0. The maximum $\bar{x}_k$ for each Q_0 is shown at the upper right of each panel.

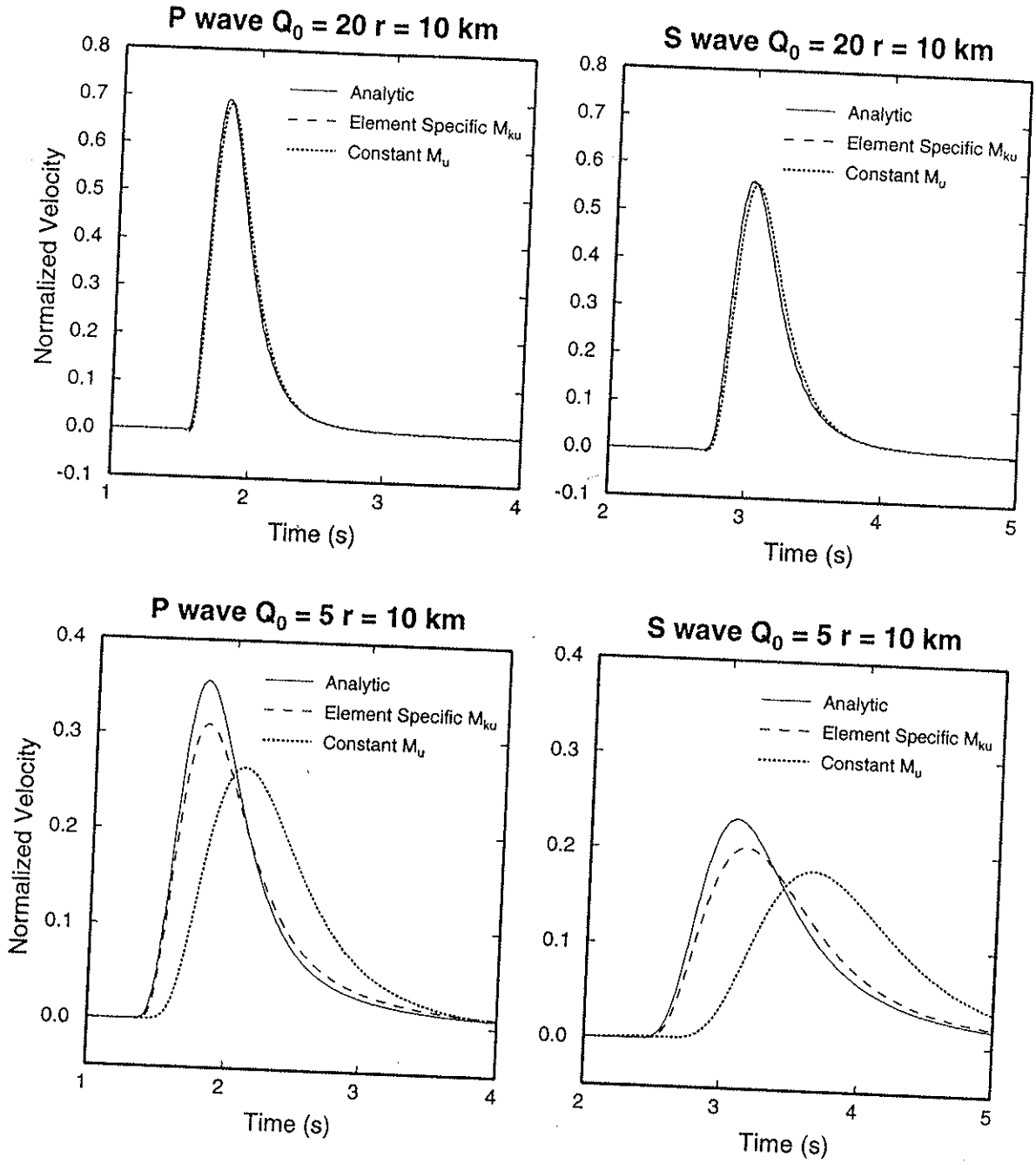

Figure 5: Waveform comparison for plane P wave (left panels) and S wave (right panels) calculations with target Q_0 values of 20 (upper panels) and 5 (lower panels). Propagation distance is 10 km. The analytic solution (solid line) is from Kjartansson (1979). For the coarse-grain calculations, the element specific M_{k_u} solution (dashed line) uses equation (16) to specify the unrelaxed moduli and the constant M_u solution (dotted line) uses the method of Day and Bradley (2001) to specify the unrelaxed modulus. Both coarse-grain solutions use the method of Day and Bradley (2001) to specify the $\bar{x}_k$ and τ_k coefficients.

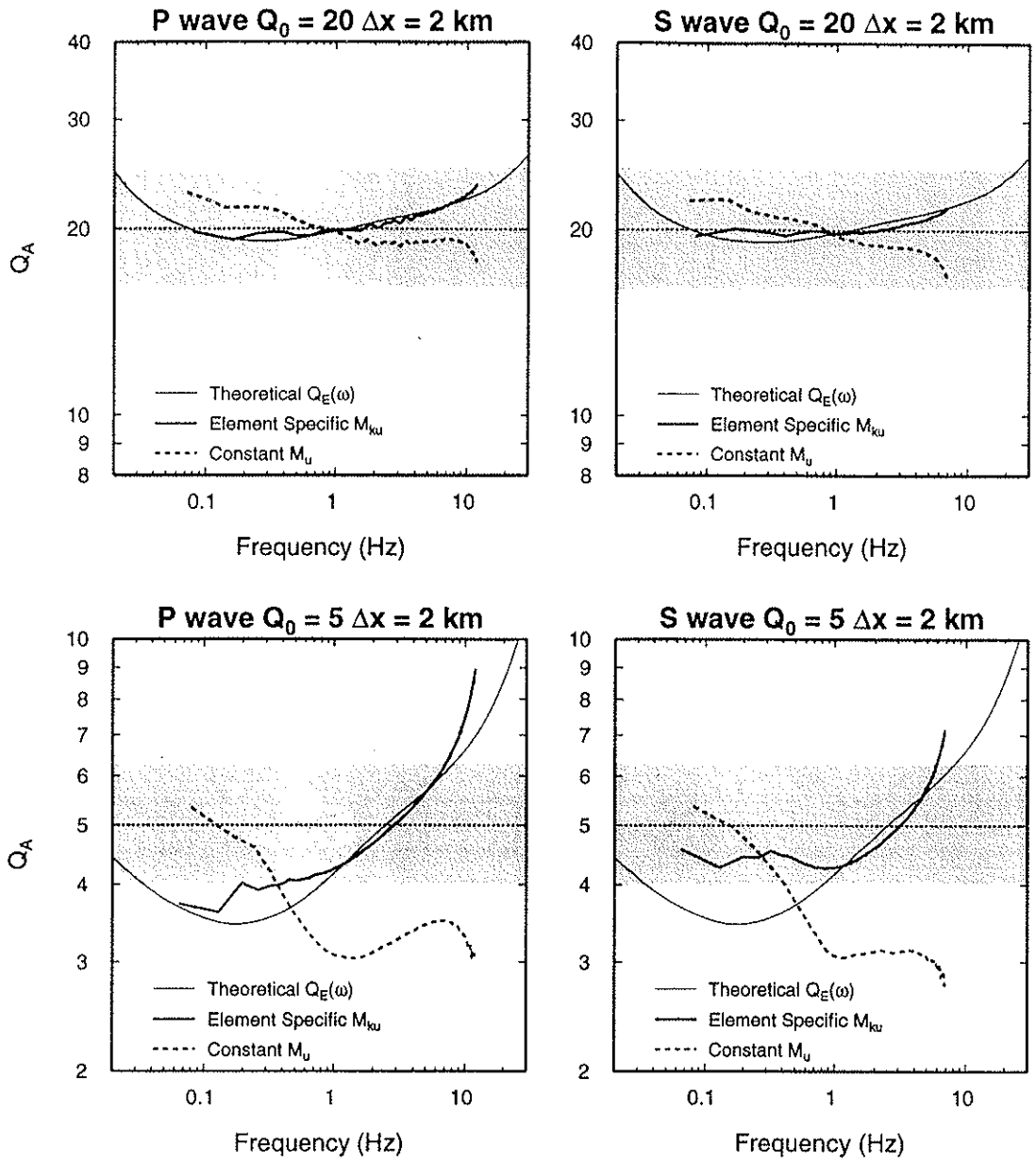

Figure 6: Apparent attenuation (Q_A) for the plane P wave (left panels) and S wave (right panels) calculations with target Q_0 values of 20 (upper panels) and 5 (lower panels). Separation distance is 2 km. The yellow shaded region represents ±25% variation around the target Q_0 value. For the coarse-grain calculations, the element specific M_{k_u} solution (red symbols) uses equation (16) to specify the unrelaxed moduli and the constant M_u solution (green symbols) uses the method of Day and Bradley (2001) to specify the unrelaxed modulus. Both coarse-grain solutions use the method of Day and Bradley (2001) to specify the $\bar{x}_k$ and τ_k coefficients. Also shown are theoretical $Q_E(\omega)$ curves determined from equation (A6).

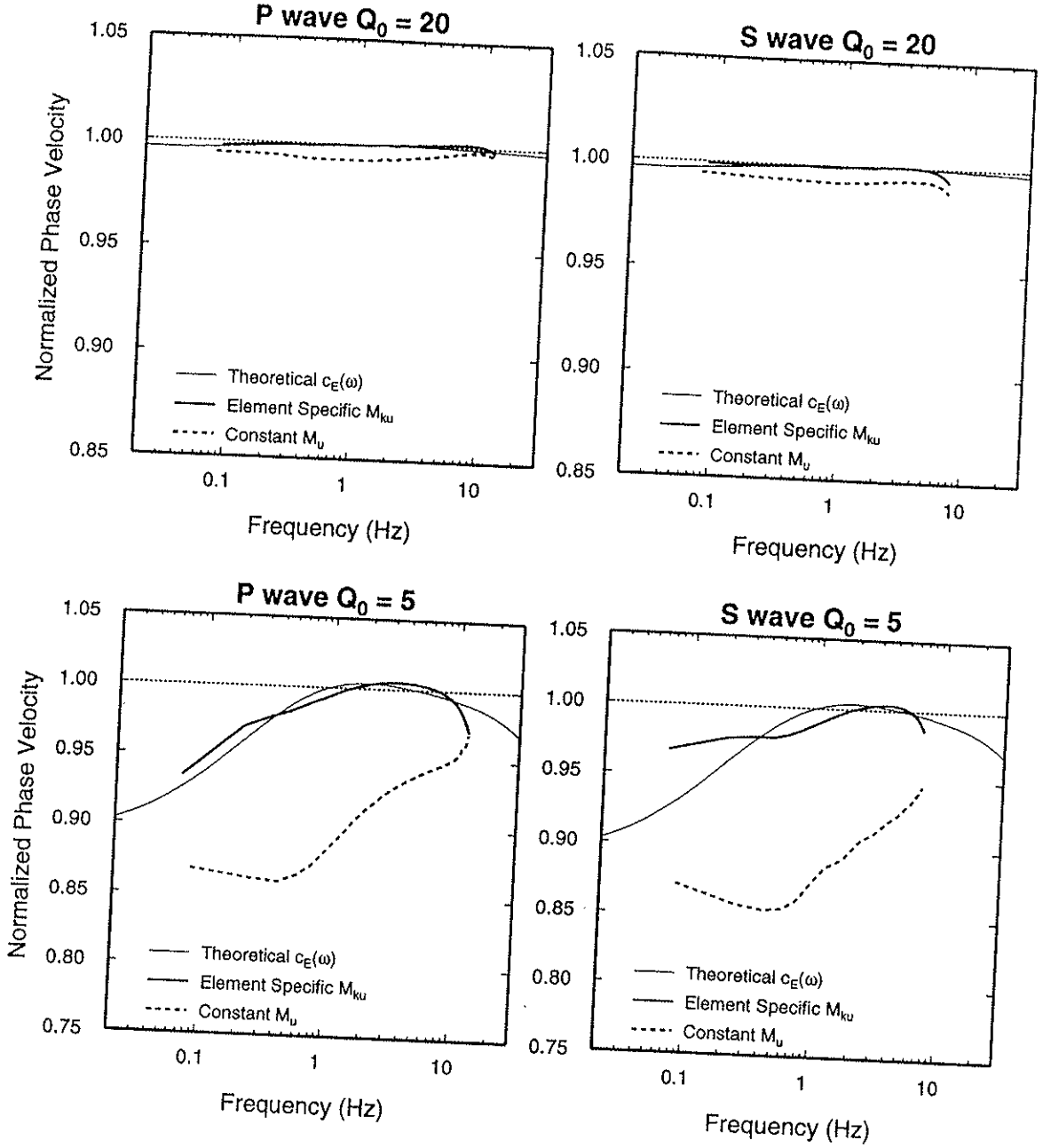

Figure 7: Normalized phase velocity measured from the plane P wave (left panels) and S wave (right panels) calculations with target Q_0 values of 20 (upper panels) and 5 (lower panels). For the coarse-grain calculations, the element specific M_{k_u} solution (red symbols) uses equation (16) to specify the unrelaxed moduli and the constant M_u solution (green symbols) uses the method of Day and Bradley (2001) to specify the unrelaxed modulus. Both coarse-grain solutions use the method of Day and Bradley (2001) to specify the $\bar{x}_k$ and τ_k coefficients. Also shown are theoretical $c_E(\omega)$ curves determined from equations (15) and (A5).

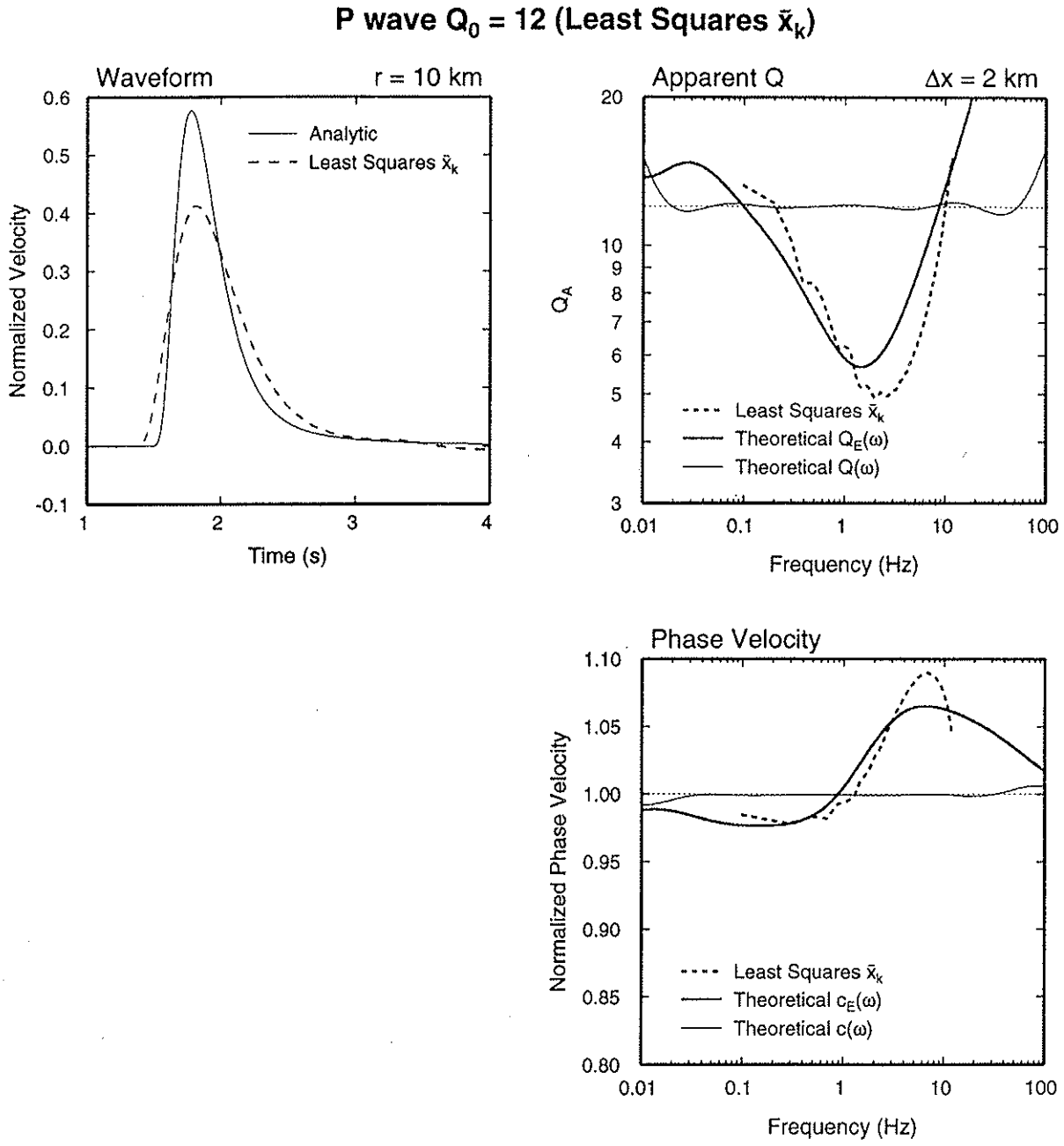

Figure 8: Theoretical and calculated waveform (upper left), Q_A (upper right) and phase velocity (lower right) comparisons for the plane P wave model with $Q_0 = 12$, and using the least-squares approach of Emmerich and Korn (1987) to determine the $\bar{x}_k$ coefficients. Theoretical curves for the general $[Q(\omega)$ and $c(\omega)]$ and effective $[Q_E(\omega)$ and $c_E(\omega)]$ parameters are also shown in the right panels.

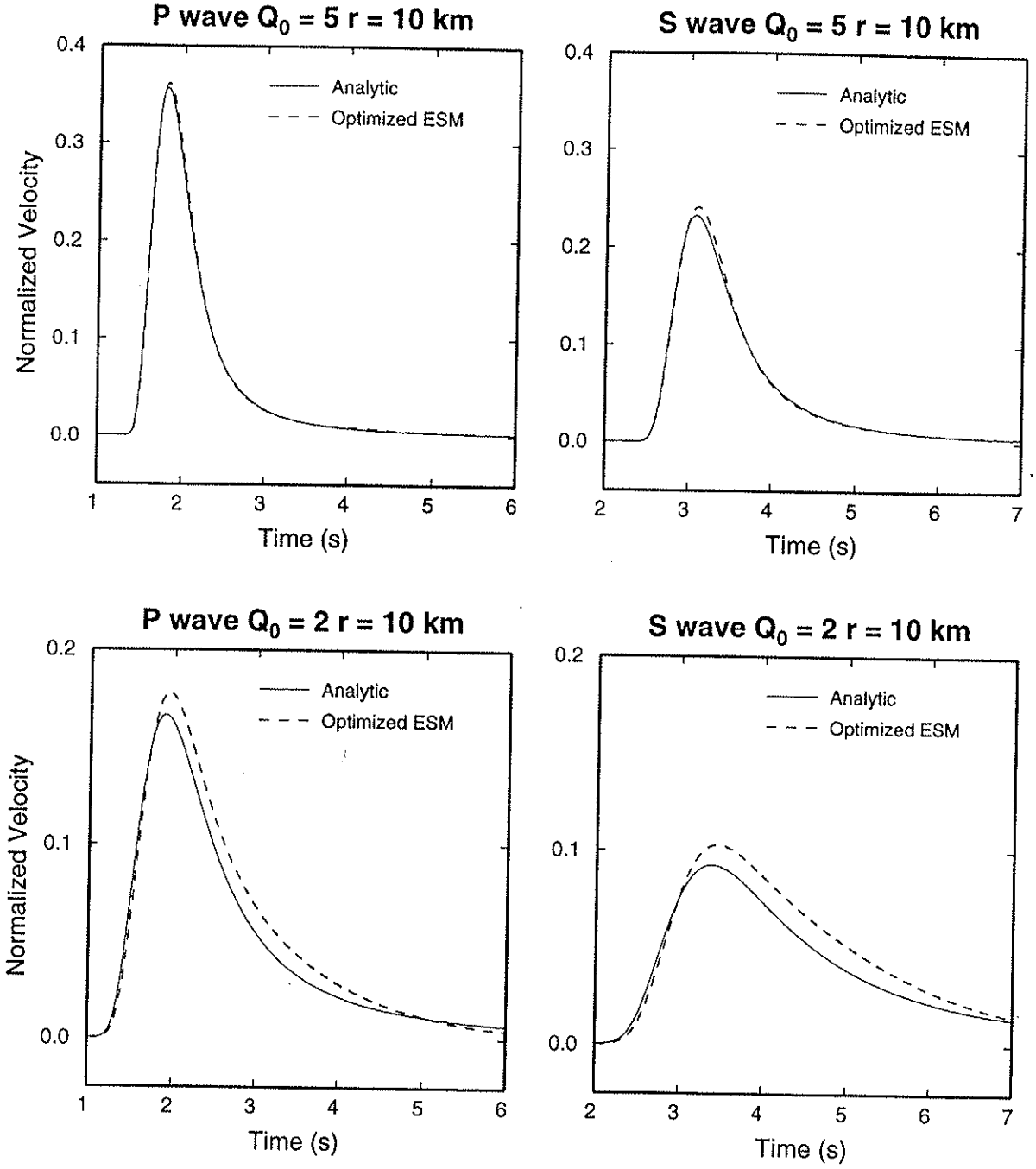

Figure 9: Waveform comparison for plane P wave (left panels) and S wave (right panels) calculations with target Q_0 values of 5 (upper panels) and 2 (lower panels). Propagation distance is 10 km. The analytic solution (solid line) is from Kjartansson (1979). For the coarse-grain calculation, the element specific M_{k_u} solution (dashed line) uses equation (16) to specify the unrelaxed moduli, and the $\bar{x}_k$ and τ_k coefficients are determined using a grid search algorithm to optimize the fit of $Q_E(\omega)$ to the target Q_0 value.

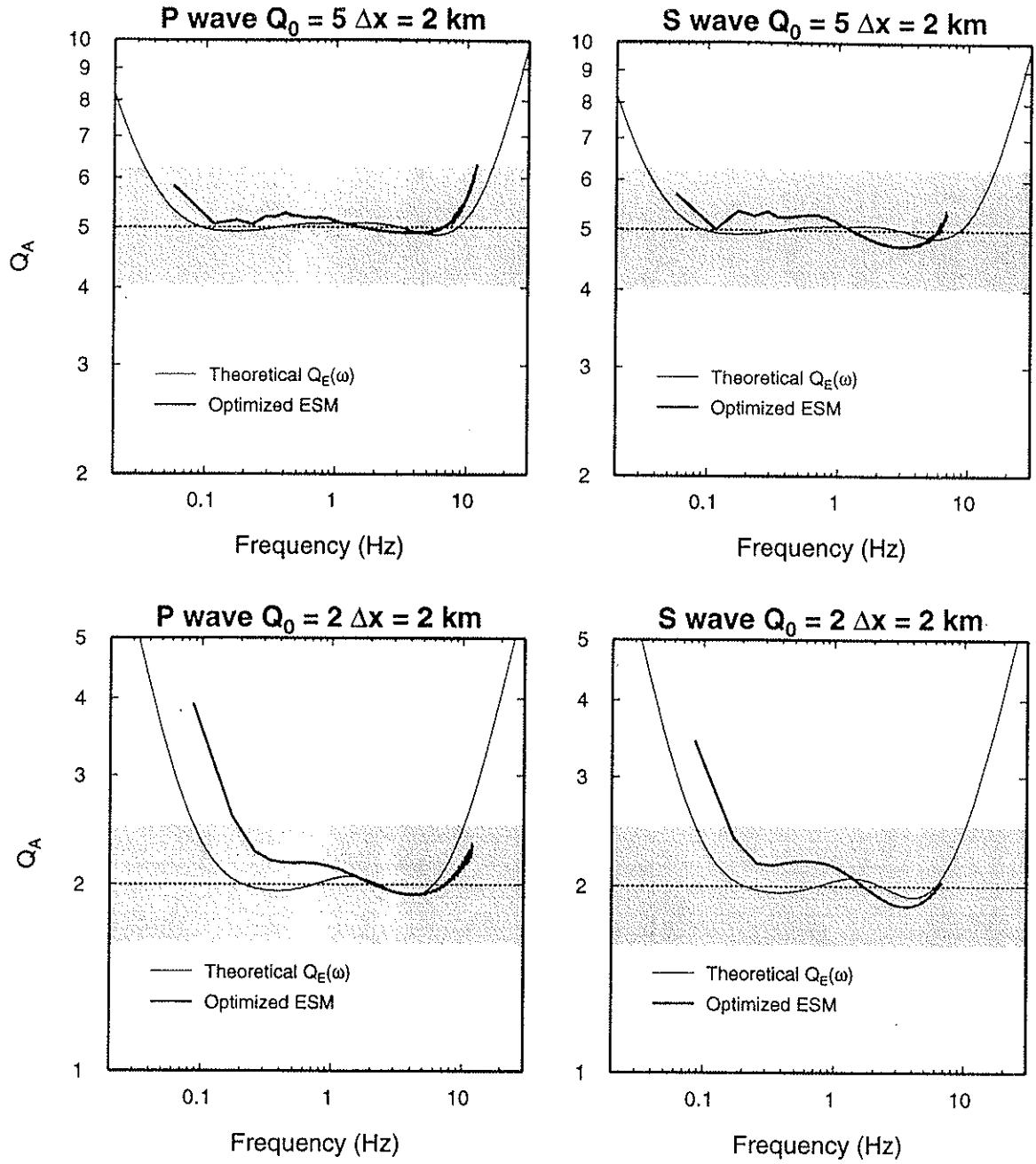

Figure 10: Apparent attenuation (Q_A) for the plane P wave (left panels) and S wave (right panels) calculations with target Q_0 values of 5 (upper panels) and 2 (lower panels). Separation distance is 2 km. The yellow shaded region represents ±25% variation around the target Q_0 value. For the coarse-grain calculation, the element specific M_{k_u} solution (red symbols) uses equation (16) to specify the unrelaxed moduli, and the $\bar{x}_k$ and τ_k coefficients are determined using a grid search algorithm to optimize the fit of $Q_E(\omega)$ to the target Q_0 value. Also shown are theoretical $Q_E(\omega)$ curves determined from equation (A6).

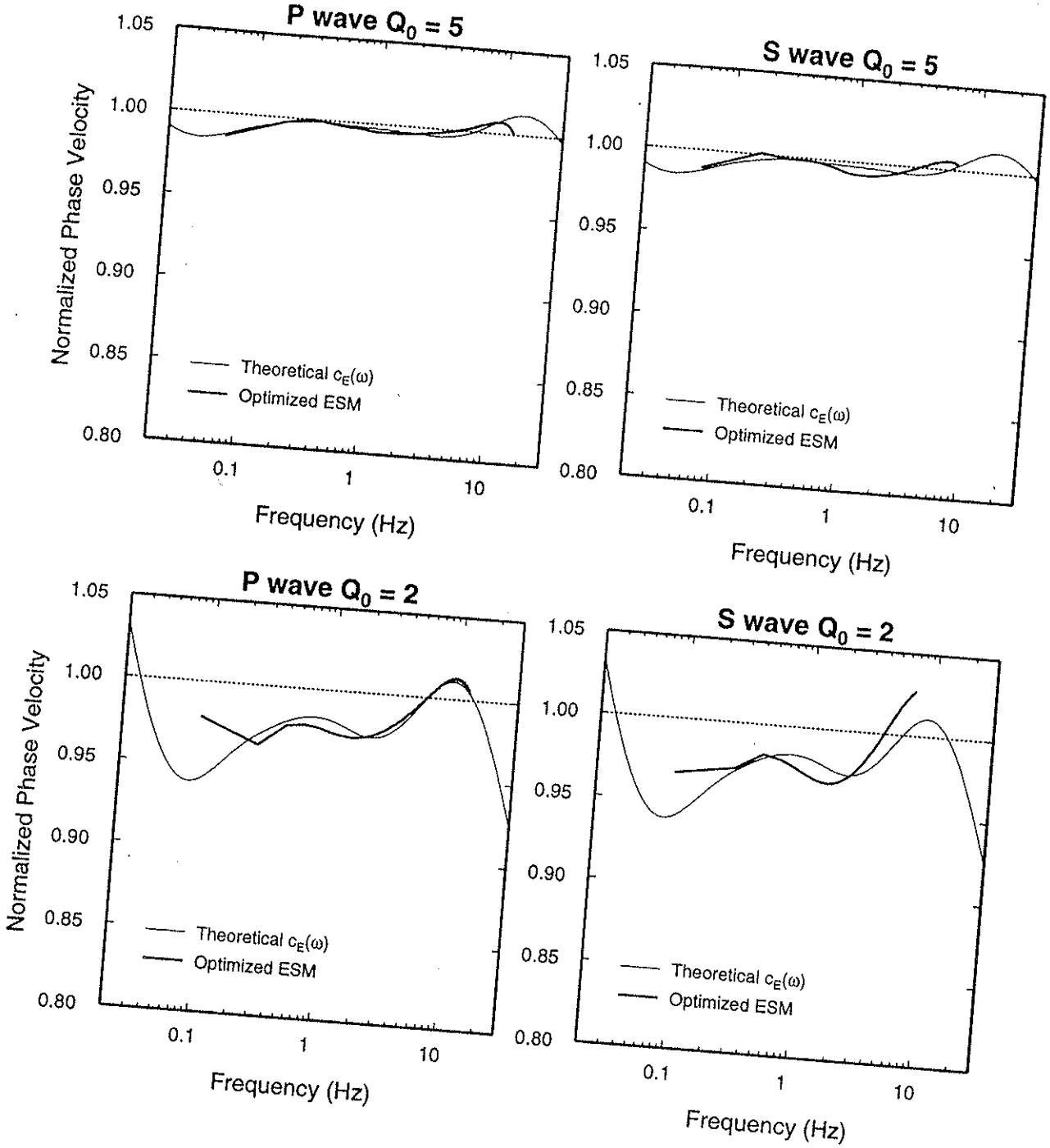

Figure 11: Normalized phase velocity measured from the plane P wave (left panels) and S wave (right panels) calculations with target Q_0 values of 5 (upper panels) and 2 (lower panels). For the coarse-grain calculations, the element specific M_{k_u} solution (red symbols) uses equation (16) to specify the unrelaxed moduli, and the $\bar{x}_k$ and τ_k coefficients are determined using a grid search algorithm to optimize the fit of $Q_E(\omega)$ to the target Q_0 value. Also shown are theoretical $c_E(\omega)$ curves determined from equations (15) and (A5).

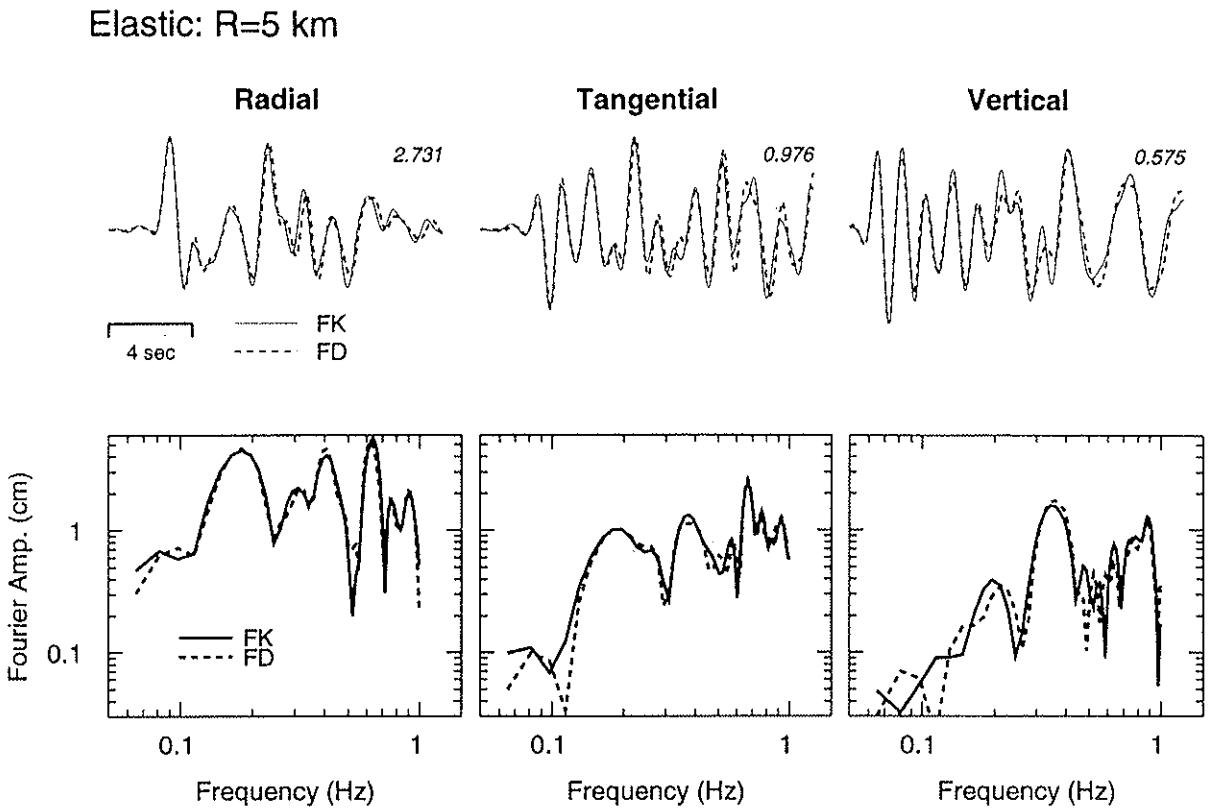

Figure 12: Comparison of FD and FK simulations for the purely elastic layered model test. Top panels show three component velocity waveforms at a range of 5 km from the source. Peak velocity for each component is indicated at upper right of each set of traces. Lower panels compare the Fourier amplitude spectra (unsmoothed) for the simulations. All results have been lowpass filtered at 1 Hz.

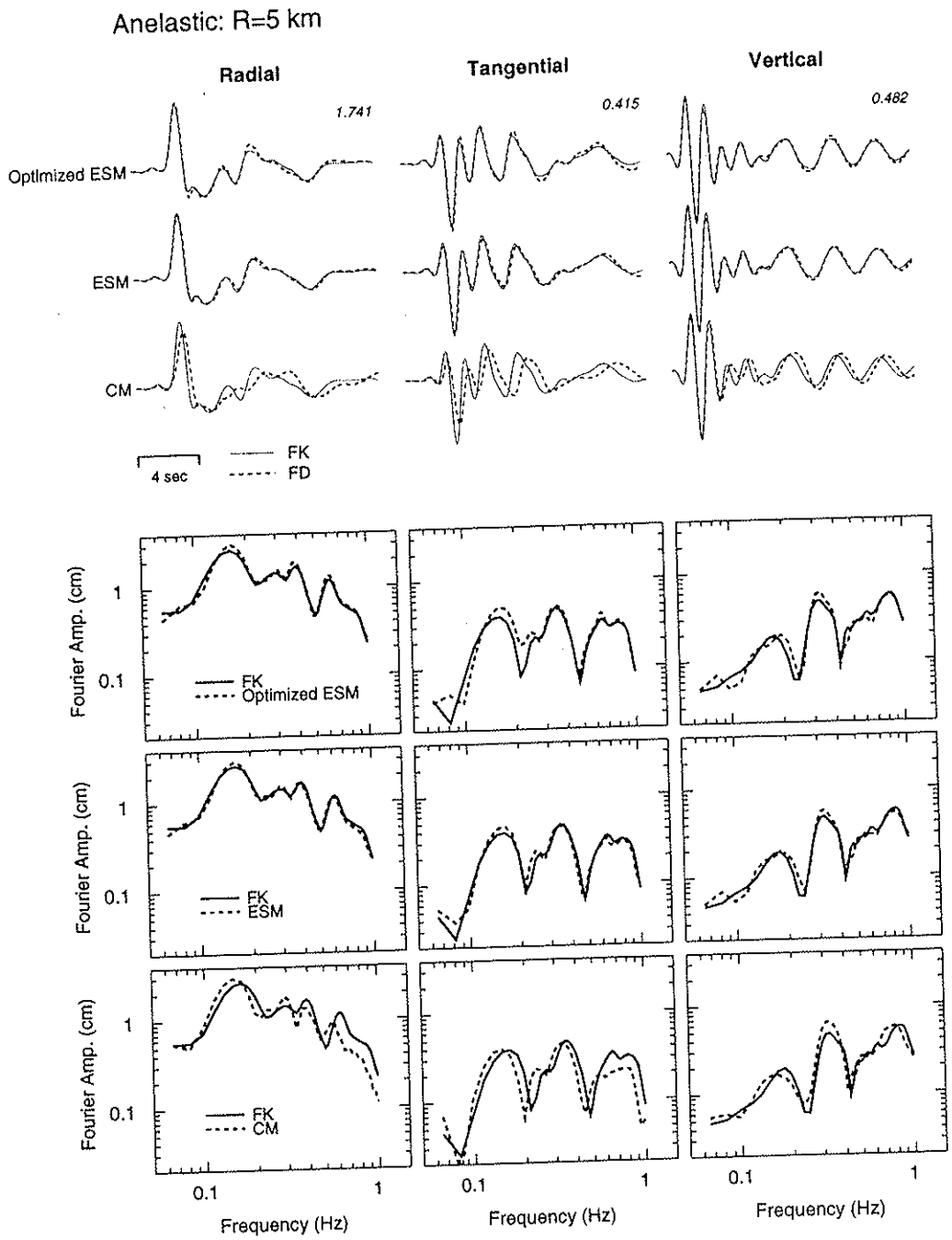

Figure 13: Comparison of FD and FK simulations for the anelastic layered model test. Three different FD simulations were performed, using respectively, the CM, ESM and Optimized ESM formulations. Top panels show three component velocity waveforms at a range of 5 km from the source. Peak velocity for each component is indicated at upper right of each set of traces. Lower panels compare the Fourier amplitude spectra (unsmoothed) for the simulations. All results have been lowpass filtered at 1 Hz.